Supporting Information for:

Cp* Non-innocence Leads to a Remarkably Weak C−H Bond via Metallocene Protonation

Matthew J. Chalkley, Paul H. Oyala,* and Jonas C. Peters*

Division of Chemistry and Chemical Engineering, California Institute of Technology (Caltech), Pasadena, California 91125, United States

Contents:

S.1 General Procedures:

General Considerations: All manipulations were carried out using standard Schlenk or glovebox techniques under an N_2 atmosphere. Unless otherwise noted, solvents were deoxygenated and dried by thoroughly sparging with N_2 gas followed by passage through an activated alumina column in the solvent purification system by SG Water, USA LLC. Non-halogenated solvents were tested with a standard purple solution of sodium benzophenone ketyl in tetrahydrofuran in order to confirm effective oxygen and moisture removal. All reagents were purchased from commercial vendors and used without further purification unless otherwise stated. $Cp^*{}_2Co$,[1] $Cp^*(\eta^4\text{-}C_5Me_6Co)$,[2] $[H(OEt_2)_2][BAr^F{}_4]$ ($HBAr^F{}_4$, $BAr^F{}_4$ = tetrakis-(3,5-bis(trifluoromethyl)phenyl)borate),[3] $[Fc][BAr^F{}_4]$ (Fc = ferrocenium),[4] and $[TBA][BD_4]$ (TBA = tetrabutylammonium, BD_4 = borodeuteride)[5] were synthesized according to a literature procedure. Deuterated solvents were purchased from Cambridge Isotope Laboratories, Inc. C_6D_6 and MeCN-d_3 were degassed and stored over activated 3 Å molecular sieves prior to use. Elemental analysis was performed by the Beckman Institute Elemental Analysis facility at California Institute of Technology. ^1H and ^{13}C NMR chemical shifts are reported in ppm relative to tetramethylsilane, using residual solvent resonances as internal standards. Solid IR measurements were obtained on a Bruker Alpha spectrometer equipped with a diamond ATR probe.

EPR Spectroscopy: X-band (9.4 GHz) CW EPR spectra were acquired using a Bruker EMX spectrometer equipped with a Super High-Q (SHQE) resonator using Bruker Win-EPR software (ver. 3.0). Spectra were acquired at 77 K using a vacuum-insulated quartz liquid nitrogen immersion dewar inserted into the EPR resonator.

Pulse EPR Spectroscopy: All pulse Q-band (34 GHz) electron nuclear double resonance (ENDOR), hyperfine sublevel correlation (HYSCORE), and electron spin echo detected field-swept spectra were acquired using a Bruker ELEXSYS E580 pulse EPR spectrometer equipped with a Bruker D2 resonator. Temperature control was achieved using an ER 4118HV-CF5-L Flexline Cryogen-Free VT cryostat manufactured by ColdEdge equipped with an Oxford Instruments Mercury ITC temperature controller.

Q-band electron spin-echo detected EPR (ESE-EPR) field-swept spectra were acquired using the 2-pulse "Hahn-echo" sequence ($\pi/2 - \tau - \pi - \tau -$ echo) where τ was held constant. Subsequently, each field swept echo-detected EPR absorption spectrum was modified using a pseudo-modulation function to approximate the effect of field modulation and produce the CW-like 1st derivative spectrum.[6] Specific acquisition parameters: $\pi/2$ = 12 ns; π = 24 ns; τ = 160 ns (6 K spectra), 600 ns (10 K spectra); shot repetition time (srt) = 5 ms (6 K spectra), 2 ms (10 K spectra).

Q-band inversion recovery experiments were conducted using the pulse sequence $\pi - T - \pi/2 - \tau - \pi - \tau -$ echo, where T is a variable delay and τ is a fixed delay. Specific acquisition parameters: $\pi/2$ = 12 ns; π = 24 ns; τ = 160 ns

Q-band HYSCORE spectra were acquired using the 4-pulse sequence ($\pi/2 - \tau - \pi/2 - t_1 - \pi - t_2 - \pi/2 - \tau -$ echo), where τ is a fixed delay, and t_1 and t_2 are variable delays independently incremented by Δt_1 and Δt_2, respectively. Sixteen step phase cycling was utilized. The time domain spectra were baseline-corrected (third-order polynomial), apodized with a Hamming window function, zero-filled to eight-fold points, and fast Fourier-transformed to yield the frequency domain. For ^2H-^1H difference spectra, the time domain of the HYSCORE spectrum of the ^1H sample was subtracted from that of the ^2H

sample, and the same data processing procedure detailed above was used to generate the frequency spectrum.

Q-band ENDOR spectra were acquired using the Davies pulse sequence ($\pi - t_{RF} - \pi_{RF} - t_{RF} - \pi/2 - \tau - \pi -$ echo), where t_{RF} is the delay between MW pulses and RF pulses, π_{RF} is the length of the RF pulse. The RF frequency was randomly sampled during each pulse sequence. Specific acquisition parameters: $\pi/2$ = 40 ns; π_{RF} = 15 μs; t_{RF} = 2 μs; π = 80 ns; τ = 300 ; shot repetition time (srt) = 5 ms

In general, the ENDOR spectrum for a given nucleus with spin I = ½ (^{1}H) coupled to the S = ½ electron spin exhibits a doublet at frequencies (Eq 1)

$$\nu_{\pm} = \left|\frac{A}{2} \pm \nu_N\right| \tag{1}$$

Where ν_N is the nuclear Larmor frequency and A is the hyperfine coupling. For nuclei with $I \geq 1$ (^{14}N, ^{2}H), an additional splitting of the $\nu_{\pm}$ (Eq 2) manifolds is produced by the nuclear quadrupole interaction (P)

$$\nu_{\pm,m_I} = \left|\nu_N \pm \frac{3P(2m_I - 1)}{2}\right| \tag{2}$$

In HYSCORE spectra, these signals manifest as cross-peaks or ridges in the 2-D frequency spectrum which are generally symmetric about the diagonal of a given quadrant. This technique allows hyperfine levels corresponding to the same electron-nuclear submanifold to be differentiated, as well as separating features from hyperfine couplings in the weak-coupling regime ($|A| < 2|\nu_I|$) in the (+,+) quadrant from those in the strong coupling regime ($|A| > 2|\nu_I|$) in the (−,+) quadrant. The (−,−) and (+,−) quadrants of these frequency spectra are symmetric to the (+,+) and (−,+) quadrants, thus typically only two of the quadrants are typically displayed in literature.

For systems with appreciable hyperfine anisotropy in frozen solutions or solids, HYSCORE spectra typically do not exhibit sharp cross peaks, but show ridges that represent the sum of cross peaks from selected orientations at the magnetic field position at which the spectrum is collected. The length and curvature of these correlation ridges allow for the separation and estimation of the magnitude of the isotropic and dipolar components of the hyperfine tensor, as shown in Fig. S1.

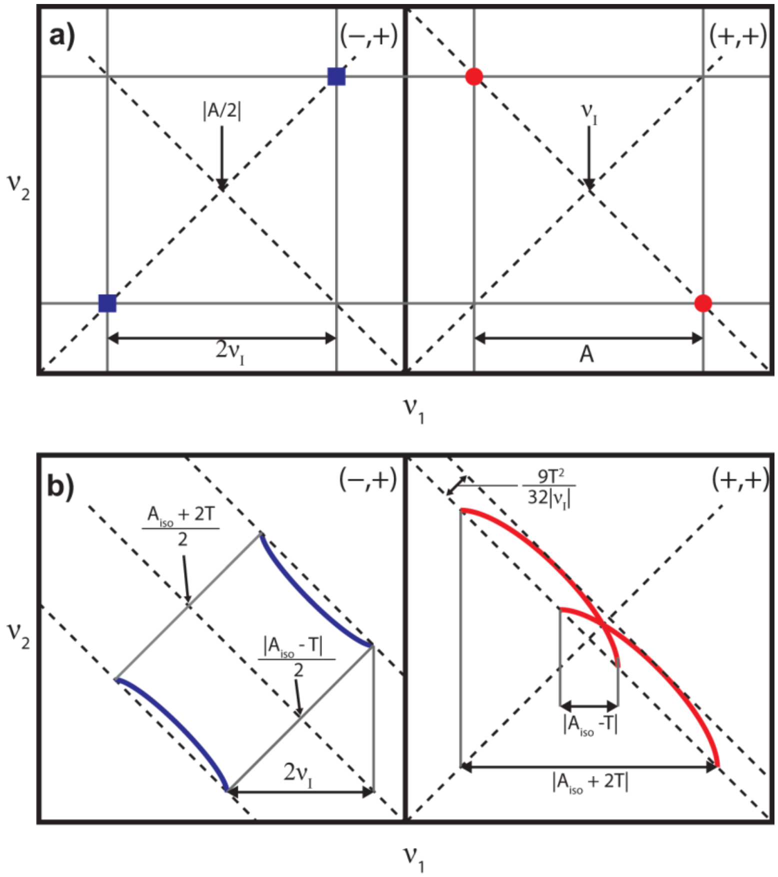

Figure S1: a) HYSCORE powder patterns for an *S* = 1/2, *I* = 1/2 spin system with an isotropic hyperfine tensor A. b) HYSCORE powder patterns for an *S* = 1/2, *I* = 1/2 spin system with an isotropic hyperfine tensor which contains isotropic (a_{iso}) and dipolar (T) contributions. Blue correlation ridges represent the strong coupling case; red correlation ridges represent the weak coupling case.

EPR simulations: All CW and pulse EPR spectra were simulated using the EasySpin[7] suite of programs with Matlab 2017 using the following Hamiltonian (Eq 3):

$$\hat{H} = \mu_B \vec{B}_0 g \hat{S} + \mu_N g_N \vec{B}_0 \hat{I} + h\hat{S}\cdot\boldsymbol{A}\cdot\hat{I} + h\hat{I}\cdot\boldsymbol{P}\cdot\hat{I} \tag{3}$$

In this expression, the first term corresponds to the electron Zeeman interaction term where μ_B is the Bohr magneton, g is the electron spin g-value matrix with principle components **g** = [g_{xx}, g_{yy}, g_{zz}], and $\hat{S}$ is the electron spin operator; the second term corresponds to the nuclear Zeeman interaction term where μ_N is the nuclear magneton, g_N is the characteristic nuclear **g**-value for each nucleus (e.g. ^{1}H, ^{2}H, ^{31}P) and $\hat{I}$ is the nuclear spin operator; the third term corresponds to the electron-nuclear hyperfine term, where A is the hyperfine coupling tensor with principle components A = [A_{xx}, A_{yy}, A_{zz}]; and for nuclei with $I \geq 1$, the final term corresponds to the nuclear quadrupole (NQI) term which arises from the interaction of the nuclear quadrupole moment with the local electric field gradient (efg) at the nucleus, where $\boldsymbol{P}$ is the quadrupole coupling tensor. In the principle axis system (PAS), $\boldsymbol{P}$ is traceless and parametrized by the quadrupole coupling constant e^2qQ/h and the asymmetry parameter η such that (Eq 4):

$$\boldsymbol{P} = \begin{pmatrix} P_{xx} & 0 & 0 \\ 0 & P_{yy} & 0 \\ 0 & 0 & P_{zz} \end{pmatrix} = \frac{e^2Qq/h}{4I(2I-1)} \begin{pmatrix} -(1-\eta) & 0 & 0 \\ 0 & -(1+\eta) & 0 \\ 0 & 0 & 2 \end{pmatrix} \qquad (4)$$

where $\frac{e^2qQ}{h} = 2I(2I-1)P_{zz}$ and $\eta = \frac{P_{xx}-P_{yy}}{P_{zz}}$. The asymmetry parameter may have values between 0 and 1, with 0 corresponding to an electric field gradient with axial symmetry and 1 corresponding to a fully rhombic efg.

The orientations between the hyperfine and NQI tensor principle axis systems and the **g**-matrix reference frame are defined by the Euler angles (α, β, γ).

X-Ray Crystallography: XRD studies were carried out at the Beckman Institute Crystallography Facility on a Bruker Kappa Apex II diffractometer (Mo Kα radiation). Structures were solved using SHELXS or SHELXT and refined against F^2 on all data by full-matrix least squares with SHELXL.[8] All of the solutions were performed in the Olex2 program.[9] The crystals were mounted on a glass fiber under Paratone N oil or fluorolube.

Electrochemistry: Electrochemical measurements were carried out in a thick-walled one-component electrochemical cell fitted with a Teflon stopcock and tungsten leads protruding from the top of apparatus. A CH instruments 600B electrochemical analyzer was used for data collection. A freshly-polished glassy carbon electrode was used as the working electrode, a platinum wire was used as the auxiliary electrode, and a silver wire as a reference electrode. The analyte was used in 1 mM concentration. The solvent and the concentration of the electrolyte are noted with the individual voltammograms. After the desired scans were completed, ferrocene (1 mM) was added to serve as an internal reference or the known decamethylcobaltocenium/decamethylcobaltocene couple was used as the internal reference. All reported potentials are referenced to the ferrocenium/ferrocene couple ($Fc^{+/0}$).

Calculations: All calculations were performed using the ORCA 4.0 program.[10,11] In cases where crystal structures were available these coordinates were used as the input. The calculations were performed using the TPSS (meta-GGA)[12] functional with the def2-SVP basis set was on C and H and the def2-TZVP basis set on Co[13] and Grimme-d3 dispersion correction.[14] That optimized structures represented true stationary points was checked by doing a single-point frequency calculations on the optimized structure.

For species where calculating the EPR parameters was of interest further calculations were performed in order to verify the robustness of those results. Using the structures optimized as described above additional optimizations were performed with other functionals: BP86 (GGA),[15,16] B3LYP (hybrid+GGA),[15,17,18] and TPSSH (hybrid+meta-GGA).[12,19] In all cases the ring-functionalized structures were found to be minima by means of a frequency calculation. For the Co–H structures in all cases (except with TPSS) there was a small negative frequency that did involve motion of the Co–H between the top and bottom ring suggesting that with these other functionals that this structure may only be a transition state. This is consistent with our previous observations with M06-L[20] where a Co–H structure could not be optimized.[21] In all cases the thermochemistry was very similar.

EPR parameters for the TPSS-optimized structure were calculated by doing a single point calculation on the optimized structures using CP(PPP)[22] on Co and def2-TZVP on C and H with Grid6 and TPSSH as the functional. To check the robustness of this basis set a higher level calculation was also done using CP(PPP) on Co and EPR-III[23] on C and H with grid 7. The results were very similar. Thus the EPR parameters were also calculated using CP(PPP) on Co and def2-TZVP on C and H with TPSS, BP86, and B3LYP. Lastly, the EPR parameters for the structures optimized using TPSSH, BP86, and B3LYP were all calculated via a single point calculation using TPSSH with CP(PPP) on Co and def2-TZVP on C and H with Grid6. See below for a discussion of the results.

For the calculation of thermochemical properties (reduction potential, pK_a, and hydricity) an additional solvation calculation was done using the CPCM solvation model with acetonitrile solvent to determine the solvated internal energy (E_{soln}).[24-26] Free energies of solvation were approximated using the difference in gas phase internal energy (E_{gas}) and solvated internal energy ($\Delta G_{solv} \approx E_{soln} - E_{gas}$) and the free energy of a species in solution was then calculated using the gas phase free energy (G_{gas}) and the free energy of solvation ($G_{soln} = G_{gas} + \Delta G_{solv}$).[27,28] The calculations of BDFE were done without the additional solvation correction as there is no change in charge for either reactants or products and it was found to introduce additional error in previous studies.

S.2 Synthetic Procedures:

Cp*(*exo*-η^4-C_5Me_5H)Co-[Cp^*_2Co][PF_6] (100.0 mg, 0.21 mmol) was added as a solid to a THF solution (15 mL) of [TBA][BH_4] (271.2 mg, 1.05 mmol, 5.0 equiv) in a Schlenk tube. This reaction was then heated to reflux and allowed to stir overnight. The reaction mixture was cooled to room temperature and the solvent was evaporated. The orange solid was extracted with pentane (8 x 5 mL) and filtered through an alumina plug. The solvent was then removed under reduced pressure to yield an orange solid. X-ray diffraction quality crystals were obtained by slow evaporation of a concentrated pentane solution. (Yield: 40.2 mg, 57.8%).

^{1}H NMR (RT, C_6D_6, 400 MHz): δ = 2.11 (1H, m, C(*H*)-CH_3), 1.87 (6H, s, β-C*H*$_3$), 1.65 (15H, s, Cp*), 1.42 (3H, d, ^{4}J(H-H) = 6.7 Hz, C(H)-C*H*$_3$) 0.76 (6H, d, ^{5}J(H-H) = 1.2 Hz, α-C*H*$_3$).
^{13}C{^{1}H} NMR (RT, C_6D_6, 100 MHz): δ = 87.74, 86.14, 53.21, 51.66, 17.08, 11.39, 10.21, 9.55.
IR (Thin Film): 2708 and 2612 cm^{-1} ($\nu_{C–H}$ for the ring-bound C–H).
UV/Vis (2-MeTHF): nm [cm^{-1} M^{-1}]): 463 [220], 565 [350].
Elemental Analysis: theory [C: 72.71 H: 9.46]; found [C: 72.82, H: 9.64]

See the IR spectra for a further discussion of why two stretches are observed for the C−H mode.

Cp*(*exo*-η^4-C_5Me_5D)Co-[Cp^*_2Co][PF_6] (100 mg, 0.21 mmol) and [TBA][BD_4] (275.4 mg, 1.05 mmol, 5 equiv) were added to a Schlenk tube as solids. A small stir bar and 20 mL of THF were then added. The reaction was then heated to reflux overnight. At this point the solvent was removed *in vacuo* and the solid extracted with (8 x 5 mL) pentane. This material was then filtered through alumina and the solvent was removed under reduced pressure. (Yield: 36.5 mg, 52.0%)

^{1}H NMR (RT, C_6D_6, 400 MHz): δ = 1.87 (6H, s, β-C*H*$_3$), 1.65 (15H, s, Cp*), 1.42 (3H, s, C(D)-C*H*$_3$) 0.76 (6H, s, α-C*H*$_3$). A small residual peak from the protio-incorporated material can be observed at 2.11 ppm. Integration of this peak suggests that there has been ~95% deuterium incorporation.
^{13}C{^{1}H} NMR (RT, C_6D_6, 100 MHz): δ = 51.21 (t, ^{2}J(C-D) = 18.0 Hz).
^{2}H{^{1}H} NMR (RT, 90% C_6H_6:10% C_6D_6, 61.42 MHz): δ = 2.05 (s).
IR (Thin Film): 2001 and 1957 cm^{-1} ($\nu_{C–D}$ for the ring-bound C–H).

Cp*(*exo*-η^4-C$_5$Me$_5$^{13}Me)Co-Cp*$_2$Co (50 mg, 0.15 mmol) was dissolved in toluene and chilled to −78 °C with stirring. To this was added dropwise ^{13}C-MeOTf (75 mg, 0.45 mmol, 3 eq). The reaction was stirred for one hour at −78 °C followed by warming to room temperature for five hours. The reaction was then filtered to remove [Cp*$_2$Co][OTf]. The desired product could then be obtained by evaporation. (Yield: 23.1 mg, 87%)

^{1}H NMR (RT, C_6D_6, 400 MHz): δ = 1.84 (6H, s), 1.65 (15H, s, Cp*), 1.42 (3H, d, ^{3}J(C-H) = 4.5 Hz) 0.76 (6H, s), 0.47 (3H, d, ^{1}J(C-H) = 124.4 Hz).
^{13}C{^{1}H} NMR (RT, C_6D_6, 100 MHz): δ = 26.38.

S.3 NMR Characterization of New Species:

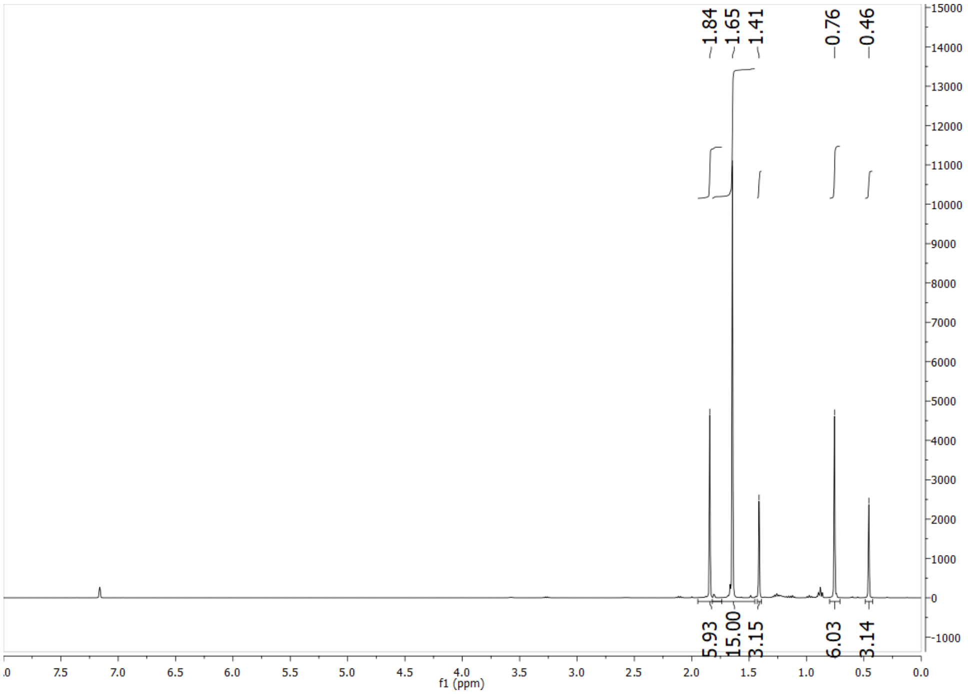

Figure S2: ^{1}H NMR spectrum (400 MHz, C_6D_6, 25 °C) of Cp*(*exo*-η^4-C$_5$Me$_5$H)Co.

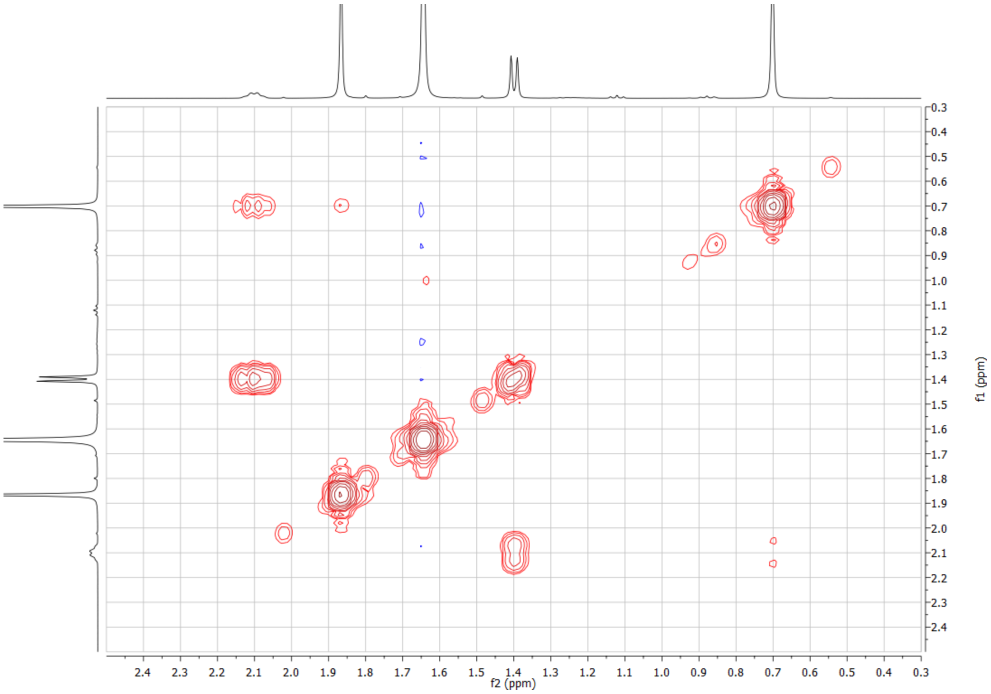

Figure S3: ^{1}H-COSY NMR spectrum (400 MHz, C_6D_6, 25 °C) of Cp*(*exo*-η^4-C_5Me_5H)Co. This data was used to establish the chemical shift of the Me groups that are α and β to the quaternary carbon.

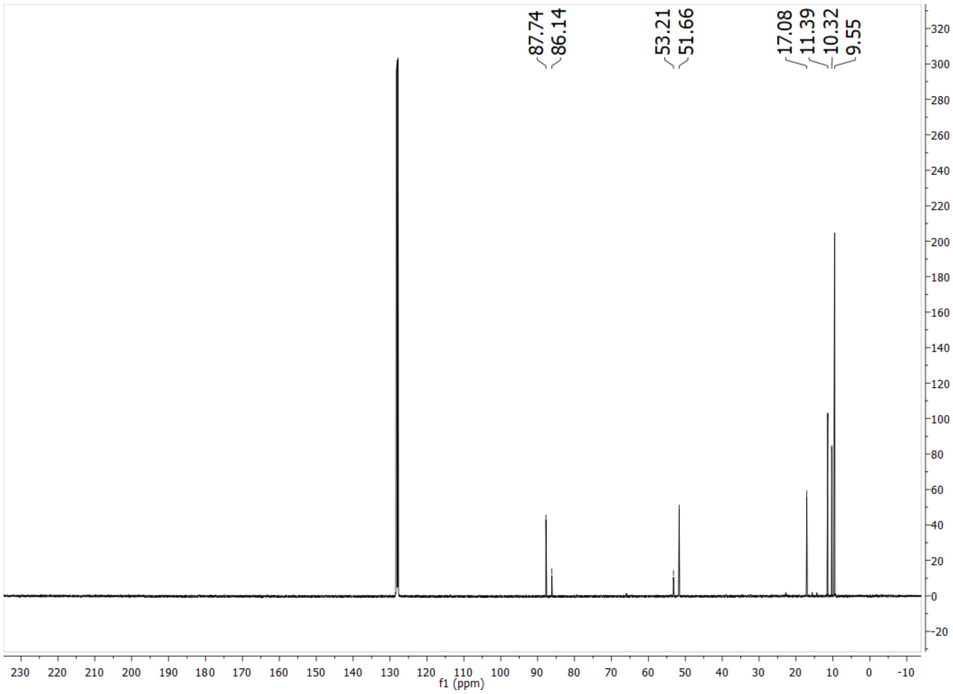

Figure S4: ^{13}C NMR spectrum (100 MHz, C_6D_6, 25 °C) of Cp*(*exo*-η^4-C_5Me_5H)Co.

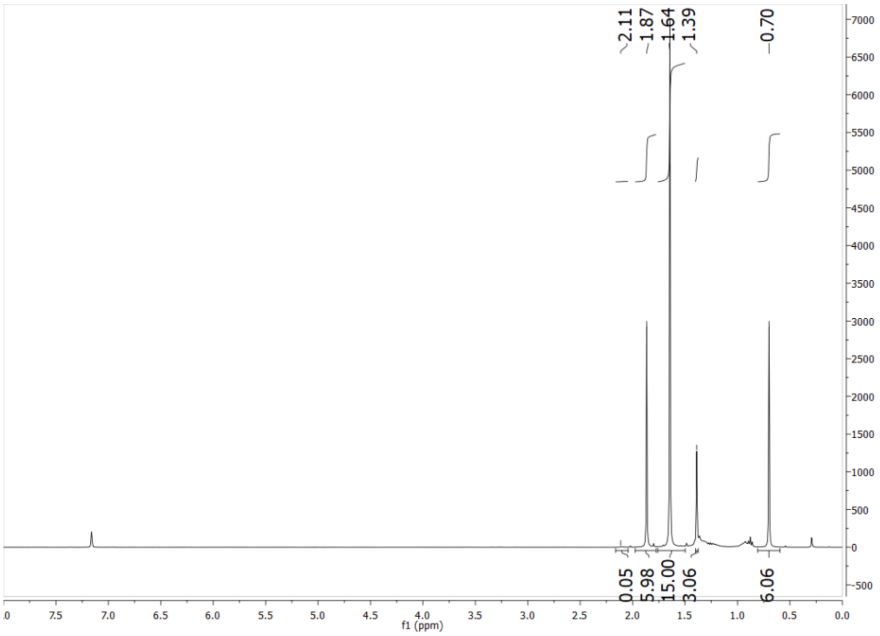

Figure S5: ^{1}H NMR spectrum (400 MHz, C_6D_6, 25 °C) of Cp*(*exo*-η^4-C_5Me_5D)Co. Integration of the residual ^{1}H signal at 2.11 i approximately 95% deuterium incorporation.

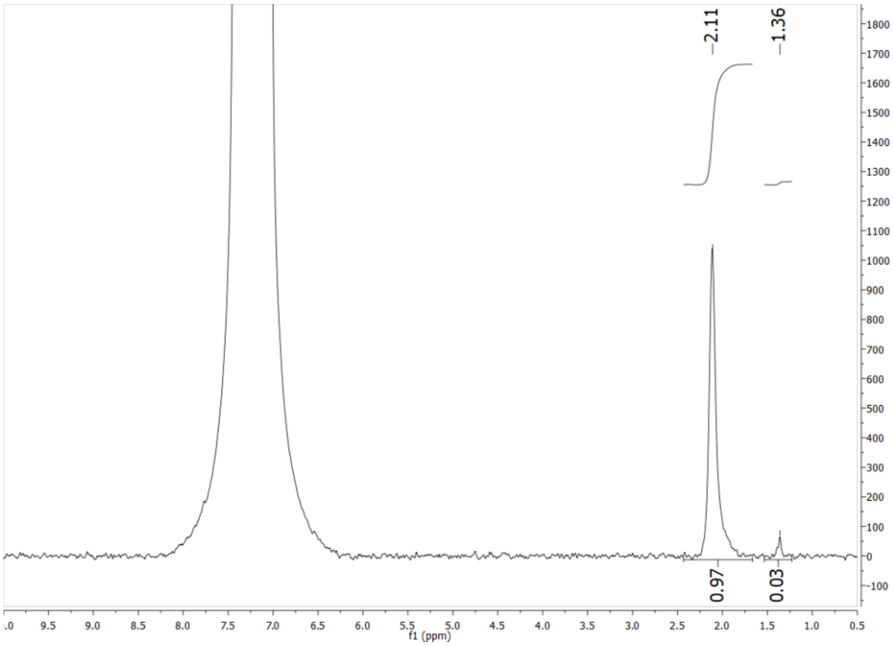

Figure S6: ^{2}H{^{1}H} NMR spectrum (61.42 MHz, 90% C_6H_6:10% C_6D_6, 25 °C) of Cp*(*exo*-η^4-C_5Me_5D)Co. In addition to the expected deuterium incorporation into the *exo*-position it appears that there is also a small amount of deuterium incorporation into the methyl group that is attached to the quaternary carbon.

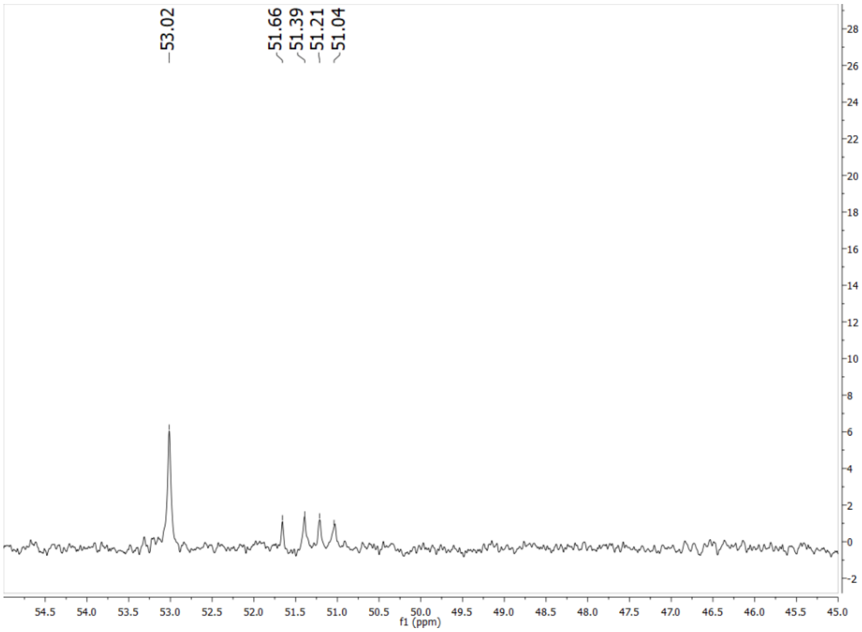

Figure S7: $^{13}C\{^{1}H\}$ NMR spectrum (100 MHz, C_6D_6, 25 °C) of Cp*(*exo*-η^4-C_5Me_5D)Co. Here we can also see a small amount of contamination with the protio species at 51.66. The triplet is centered at 51.21 demonstrating the expected change in chemical shift upon deuteration.

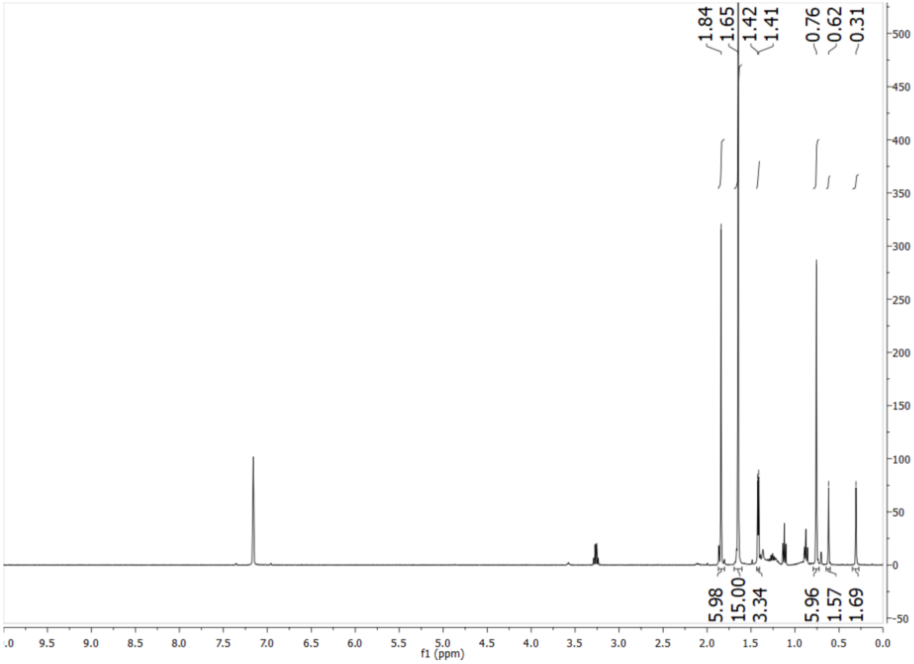

Figure S8: ^{1}H NMR spectrum (400 MHz, C_6D_6, 25 °C) of Cp*(*exo*-η^4-$C_5Me_5{}^{13}Me$)Co demonstrating the ^{13}C-^{1}H coupling evident in the splitting of the peak for the α-protons at 0.46 ppm and the smaller coupling to the γ-protons at 1.41 ppm.

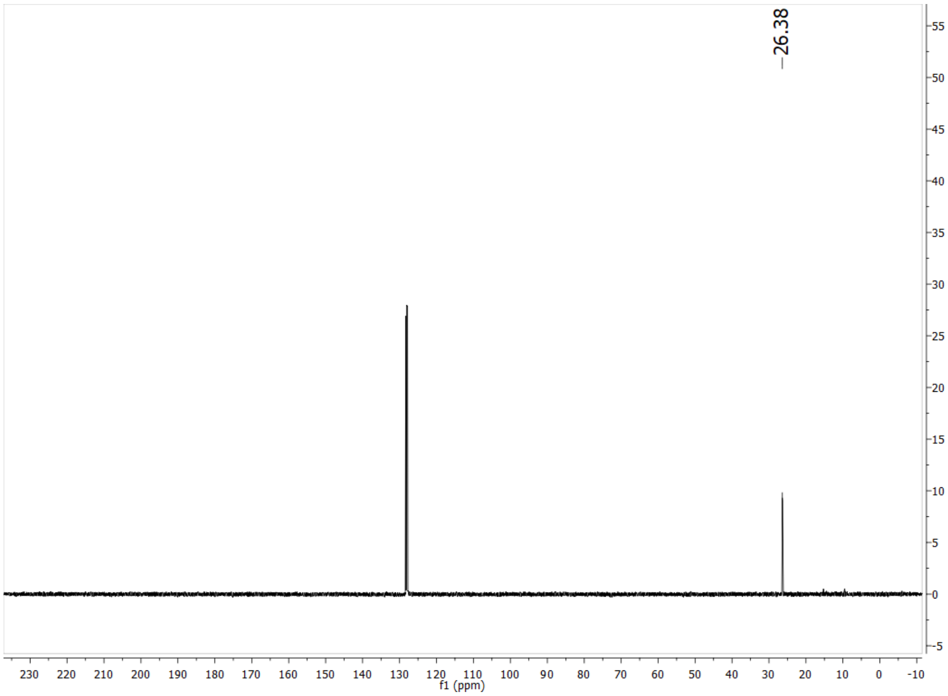

Figure S9: ^{13}C NMR spectrum (100 MHz, C_6D_6, 25 °C) Cp*(*exo*-η^4-$C_5Me_5{}^{13}Me$)Co highlighting the selective ^{13}C incorporation.

S.4 Reactivity of Cp*(*exo*-η^4-C_5Me_5H)Co:

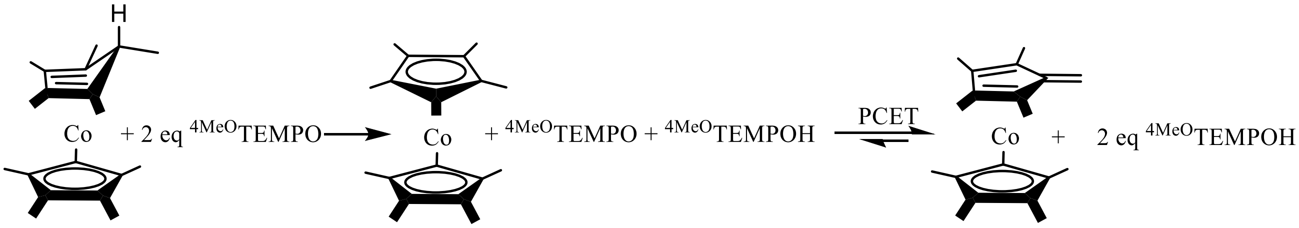

Figure S10: Reaction of Cp*(*exo*-η^4-C_5Me_5H)Co with ^{4MeO}TEMPO.

Cp*(*exo*-η^4-C_5Me_5H)Co (1.5 mg,0.005 mmol, 1 eq) and ^{4MeO}TEMPO (1.9 mg, 0.010, 2.2 eq) were dissolved in MeCN-*d*$_3$. These were then allowed to react at room temperature for thirty minutes with shaking. A ^{1}H NMR was then taken. In this the formation of 2 equivalents of ^{4MeO}TEMPOH is observed (Figure S9)[29] confirmed by integration relative to a benzene internal standard containing 2 equivalents. However, the Co product is unclear. On the basis of reactions performed in toluene, we believe that this is because of the high instability of the fulvene product, Cp*(η^4-$C_5Me_4CH_2$)Co, in coordinating solvents.

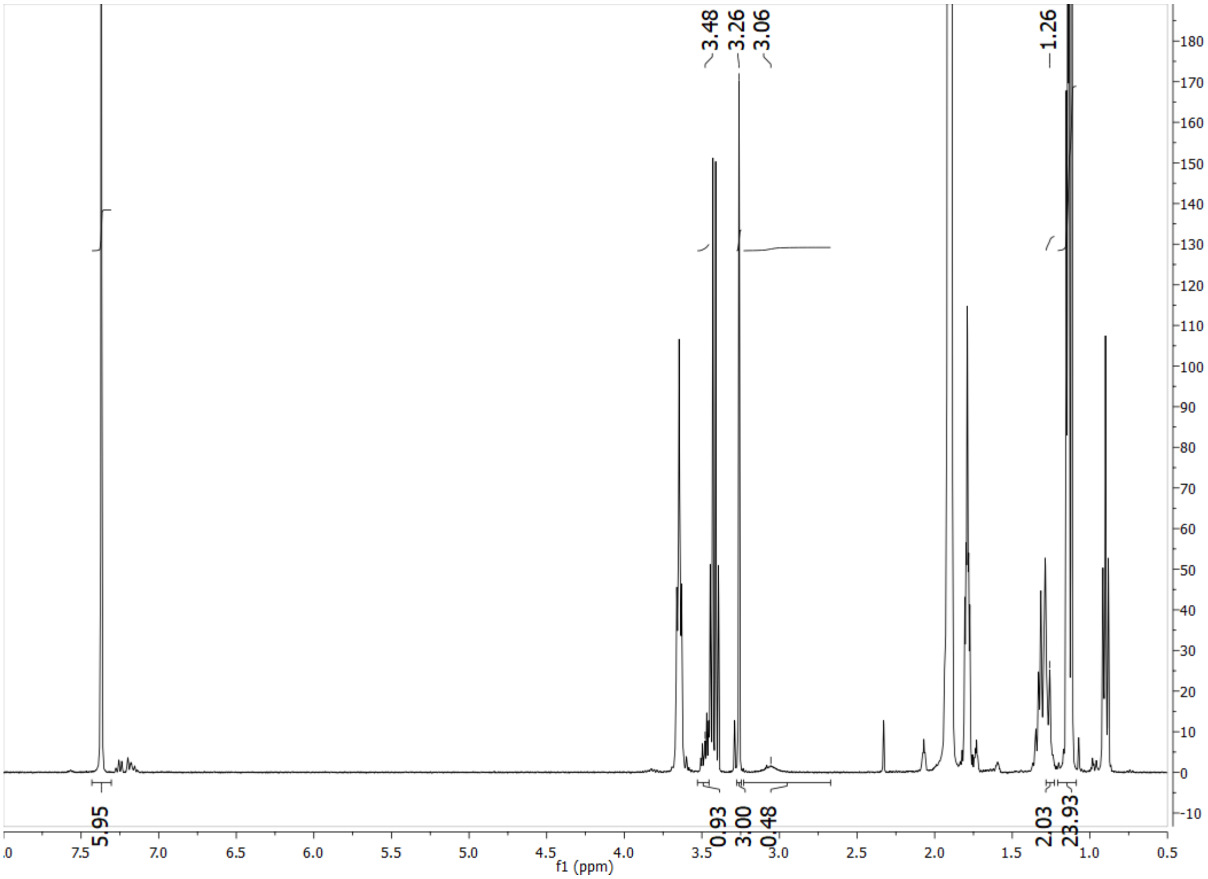

Figure S11: ^{1}H NMR spectrum (400 MHz, MeCN-*d*$_3$, RT) of the reaction between Cp*(*exo*-η^4-C$_5$Me$_5$H)Co and ^{4MeO}TEMPO.

Due to the poor solubility of the reagents in acetonitrile, the limited ability to cool that solvent, and that the NMR chemical shifts of the fulvene complex have only been previously reported in aromatic solvents the reaction was performed again in toluene-*d*$_8$.[30,31] Cp*(*exo*-η^4-C$_5$Me$_5$H)Co (4 mg, 0.012 mmol, 1 eq) and ^{4MeO}TEMPO (4.5 mg, 0.024 mmol, 1 eq) were each dissolved in minimal *d*$_8$-toluene and both added to a J-Young NMR tube (Figure S10). Due to broadening at room temperature the reaction mixture was cooled to −78 °C and a ^{1}H (Figure S11) and ^{13}C NMR were taken (Figure S13).

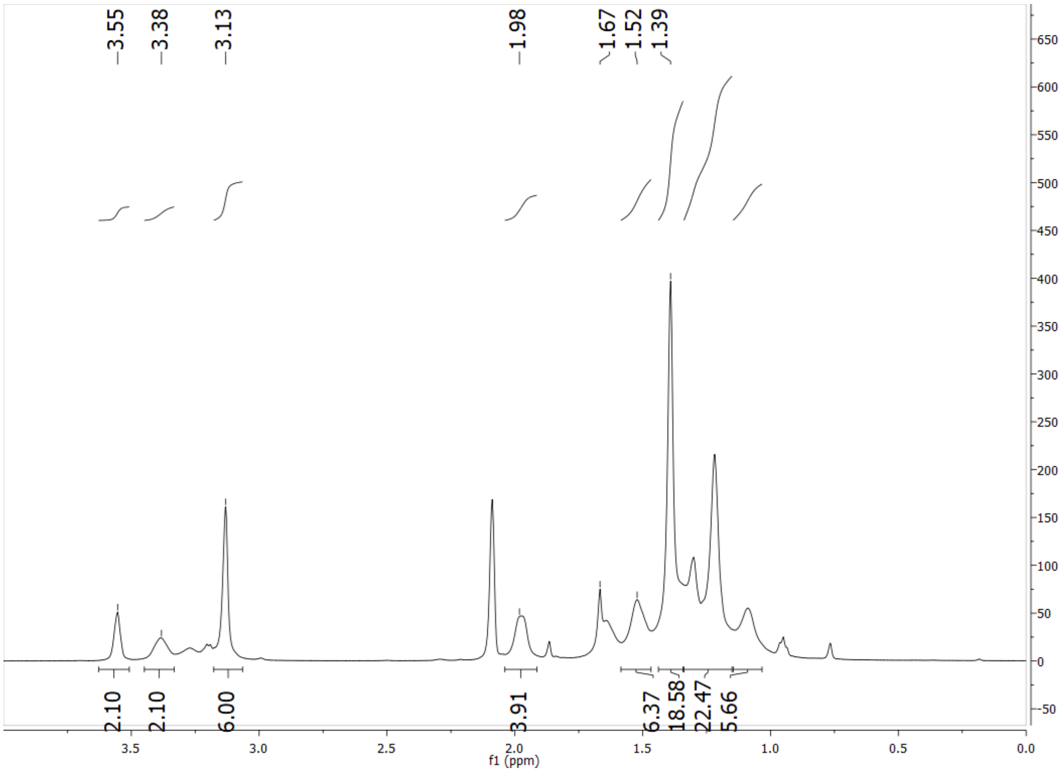

Figure S12: Zoomed in view of the ^{1}H NMR (500 MHz, C_7D_8, −78 °C) of the reaction between Cp*(*exo*-η^4-C_5Me_5H)Co and 2 equivalents of ^{4Me0}TEMPO demonstrating that two equivalents of $^{4\text{-}MeO}$TEMPOH are formed for each equivalent of Cp*(η^4-$C_5Me_4CH_2$)Co.

As further evidence for the proposed scheme, decamethylcobaltocene (8 mg, 0.024 mmol, 1 eq) and ^{4MeO}TEMPO (4.5 mg, 0.024 mmol, 1 eq) were each dissolved in minimal *d*$_8$-toluene and both added to a J-Young NMR tube (Figure S13). Due to broadening at room temperature the reaction mixture was cooled to −78 °C and a ^{1}H (Figure S14) and ^{13}C NMR were taken (Figure S16). These data are in good agreement with the previously reported spectroscopic data.[30,31] The reaction was performed in toluene-*d*$_8$ both to facilitate comparison with previous NMR data and because of the poor solubility of the reagents in MeCN.

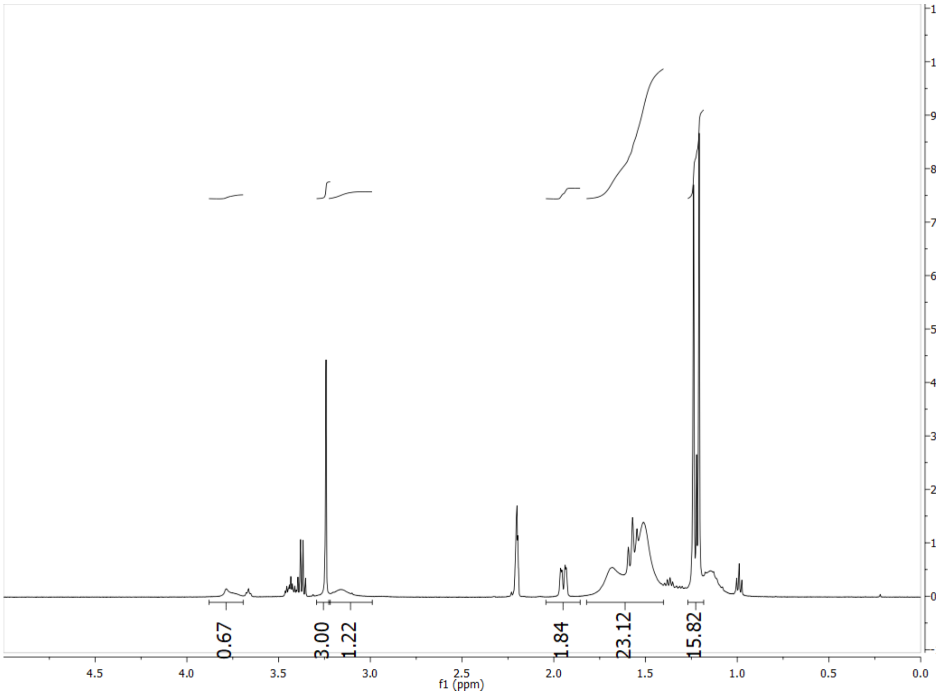

Figure S13: ^{1}H NMR spectrum (500 MHz, C_7D_8, RT) of the reaction between Cp^*_2Co and ^{4MeO}TEMPO.

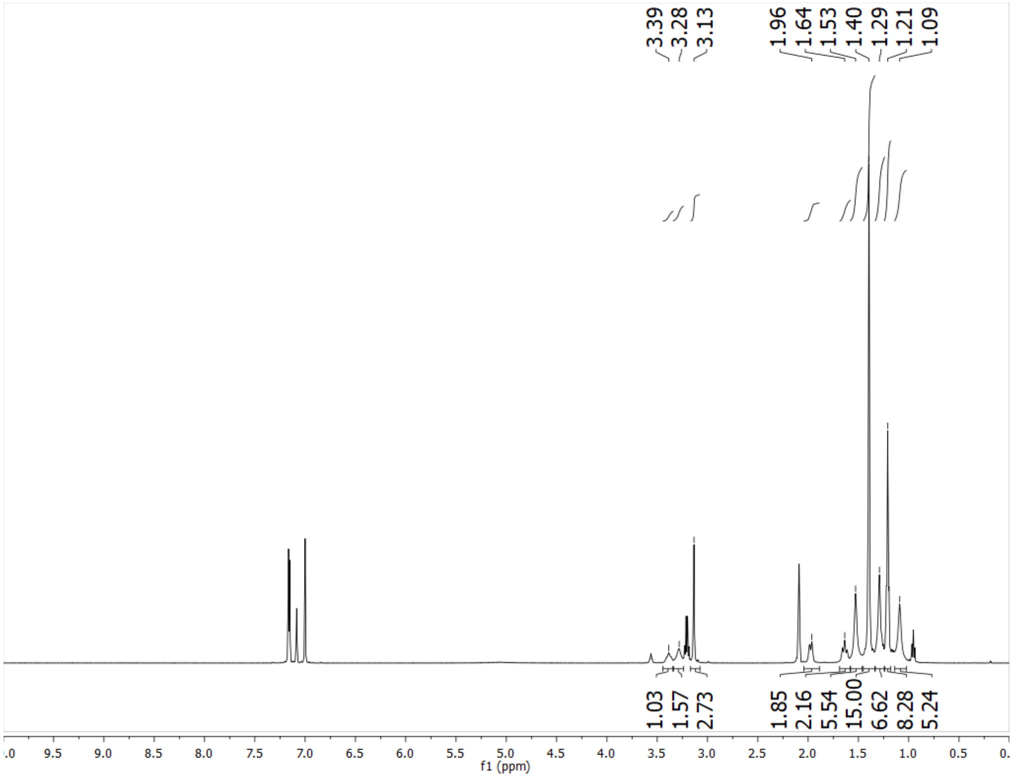

Figure S14: ^{1}H NMR spectrum (500 MHz, C_7D_8, −78 °C) of the reaction between Cp^*_2Co and ^{4MeO}TEMPO.

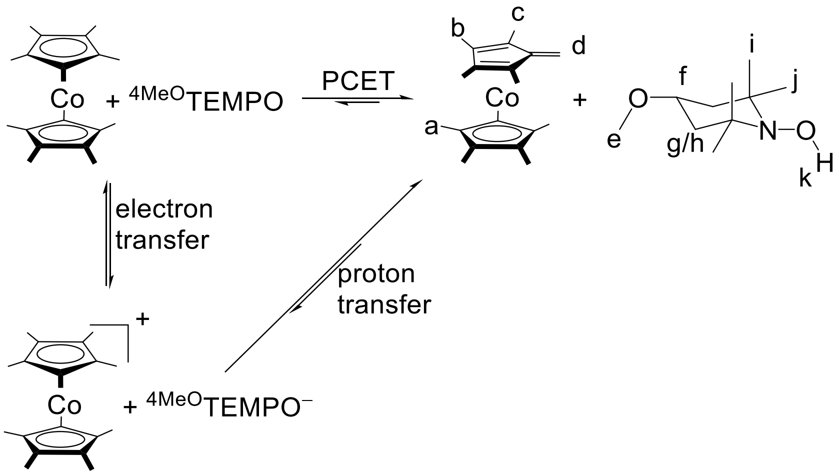

Figure S15: Reaction scheme and the left side is labeled with the assignments made in the ^{1}H NMR based on known spectroscopic properties of these molecules. Both the concerted and separated PCET reaction pathways are possible. The deprotonation of decamethylcobaltocenium by TEMPO^{-} has been observed previously as part of a more complicated reaction scheme.[31]

^{1}H NMR (−78 °C, C_7D_8, 500 MHz): δ = 5.10 (1H, s, **k**), 3.39 (1H, app t, ^{3}J(H-H) = 11.3 MHz, **f**), 3.26 (2H, s, **d**), 3.13 (3H, s, **e**), 1.98 (2H, d, ^{3}J(H-H) = 11.3 Hz, **g/h**), 1.64 (2H, t, ^{2}J(H-H) = 11.2 MHz, **g/h**), 1.53 (6H, s, **b/c**), 1.40 (15 H, s, **a**), 1.29 (6H, s, **i/j**), 1.21 (6H, s, **i/j**), 1.09 (6H, s, **b/c**).

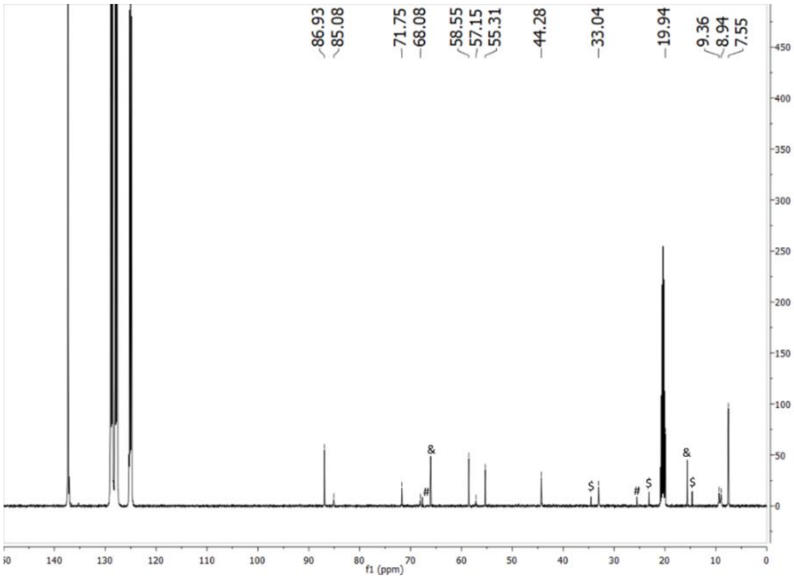

Figure S16: ^{13}C NMR spectrum (125 MHz, C_7D_8, −78 °C) of between $Cp^*{}_2Co$ and ^{4Me0}TEMPO which demonstrates the formation of $Cp^*(\eta^4\text{-}C_5Me_4CH_2)Co$ and ^{4MeO}TEMPO-H. Residual solvents are indicated with symbols (# = THF, & = diethylether, \$ = pentane).

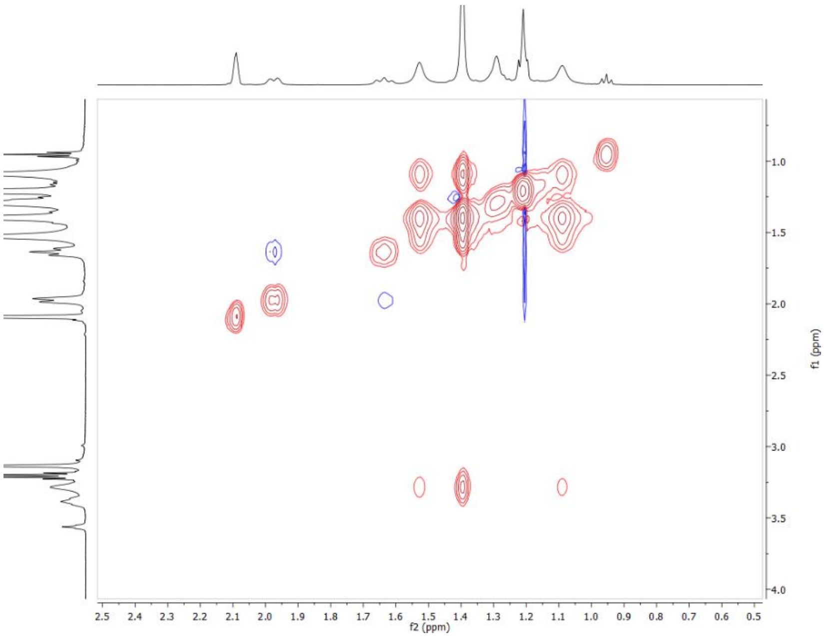

Figure S17: Zoomed in data from the ^{1}H-ROESY NMR (500 MHz, C_7D_8, −78 °C) of the reaction between Cp*$_2$Co and $^{4\text{Me0}}$TEMPO.

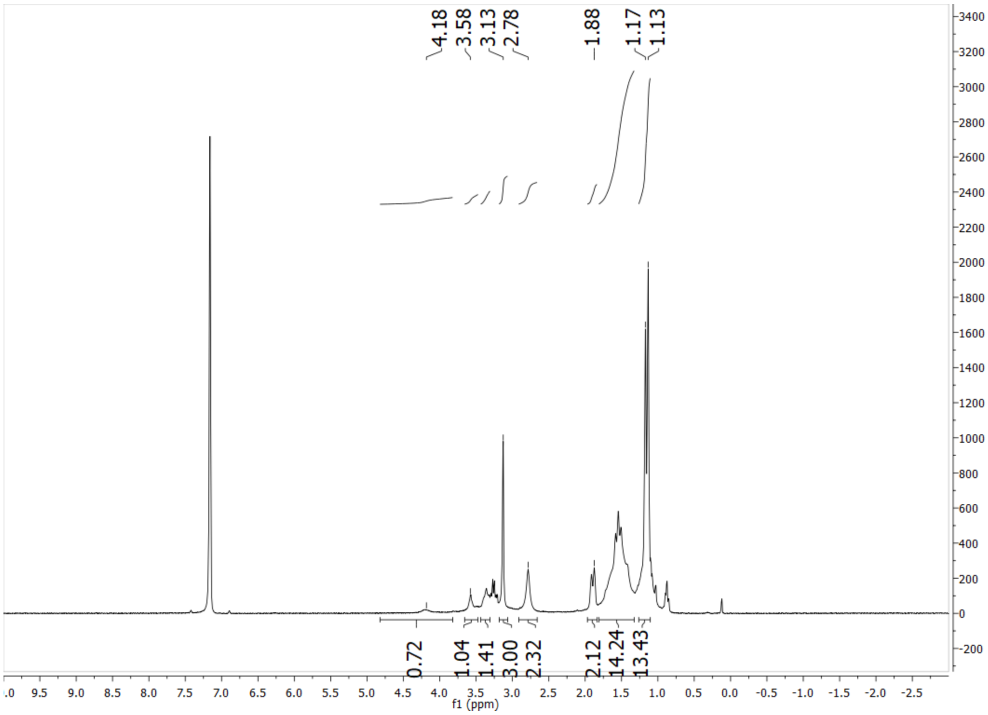

Figure S18: ^{1}H NMR spectrum (400 MHz, C_7D_8, RT) of the reaction between octamethylcobaltocene (4 mg, 0.013 mmol, 1 eq) and $^{4\text{MeO}}$TEMPO (2.5 mg, 0.013 mmol, 1 eq).

In the ROESY NMR spectrum at −78 °C (Figure S17), there is clear chemical exchange between the different positions of the fulvene complex. The ROESY experiment is phase-sensitive, so you can observe both the through-space interaction between the axial and equatorial protons on the piperidin-1-oxyl ring, and the exchange coupling between all the positions that originate from the Cp*$_2$Co species. The lack of through space interaction between the resonances from the ^{4MeO}TEMPO-H and those from the Cp*Co-derived fragment suggest that they are not coupled. However, the exchange between the resonances attributed to Cp*(η^4-$C_5Me_4CH_2$)Co along with the broadening at room temperature indicates that the reaction between these two is reversible with two possibilities shown in Figure S15. The observation of similar reactivity between ^{4MeO}TEMPO and octamethylcobaltocene (Figure S18) biases us towards the latter explanation but does not provide definitive evidence.

This reversibility is not evident in acetonitrile. This may be because the O–H bond is stronger in this more polar solvents due to preferential hydrogen bonding interactions relative to the C–H bond of the methyl in Cp*$_2$Co. It has been observed that the O–H bond of TEMPO–H is a little more than 1 kcal mol^{-1} stronger in acetonitrile than in benzene.

Attempts to isolate the fulvene product from this reaction were precluded by the similar solubility of the two products and as had been previously observed, the relative instability of this complex at room temperature.

Reaction of Cp*(*exo*-η^4-C_5Me_5H)Co with CO_2: Cp*(*exo*-η^4-C_5Me_5H)Co (2.0 mg, 0.006 mmol) is dissolved in MeCN-*d$_3$* and added to a J-Young NMR tube. The J-Young tube is freeze-pump-thawed 3x and then backfilled with CO_2 that is passed through a dry-ice/acetonitrile bath to one atmosphere of pressure. The reactions is then rotated for three days and a pale yellow color is obtained. A new ^{1}H NMR reveals the formation of [Cp*$_2$Co][HCO_2] (Figure S19). This product can be further confirmed by a thin film IR spectrum of the reaction (Figure S39).

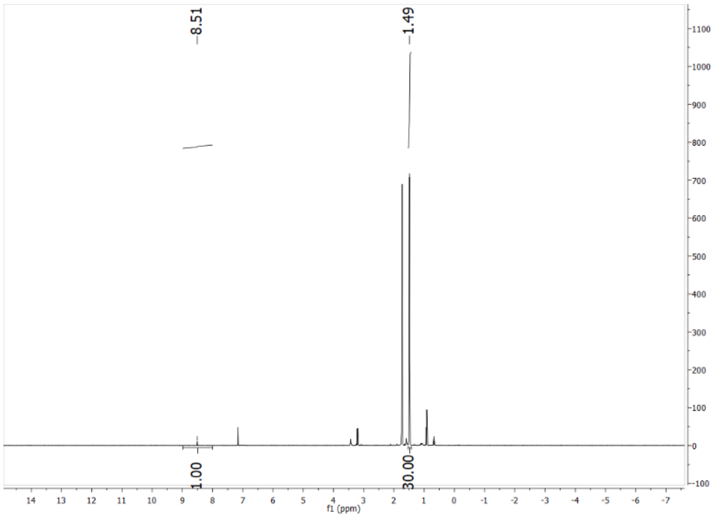

Figure S19: ^{1}H NMR (400 MHz, MeCN-*d$_3$*, RT) of the reaction of Cp*(*exo*-η^4-C_5Me_5H)Co with one atmosphere of CO_2 illustrating the formation of [Cp*$_2$Co][HCO_2] with the characteristic peak at 8.5 ppm for the formate proton.

Reaction of Cp*(*exo*-η^4-C_5Me_5H)Co with [Pt(dmpe)$_2$][PF_6]$_2$: Cp*(*exo*-η^4-C_5Me_5H)Co (1.8 mg, 0.0055 mmol) and [Pt(dmpe)$_2$][PF_6]$_2$ (9.0 mg, 0.014 mmol, 4 equiv) are added as solids to a vial. They are then dissolved in MeCN-*d$_3$* and added to a J-Young NMR tube. They are then allowed to react for one day and then a ^{1}H NMR revealed complete transfer of the hydride to the Pt to form [HPt(dmpe)$_2$][PF_6] and [Cp*$_2$Co][PF_6].

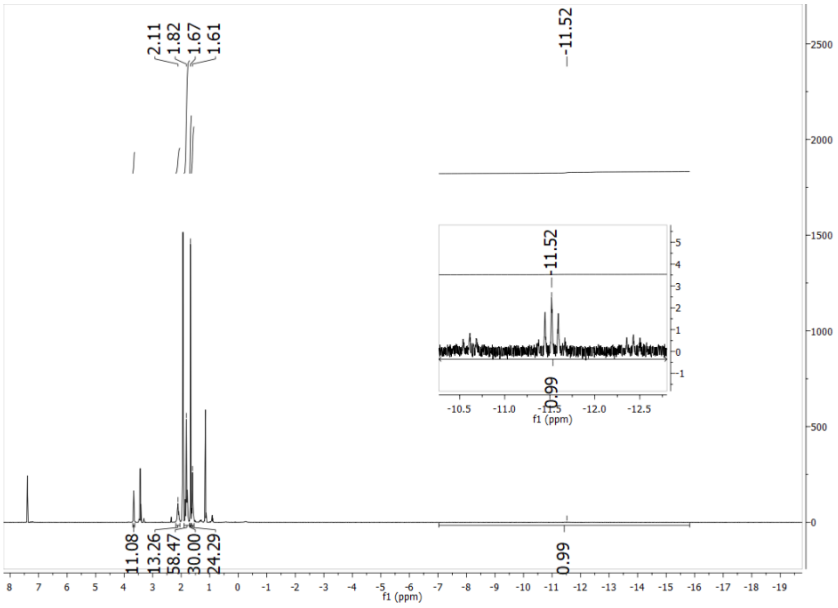

Figure S20: ^{1}H NMR (400 MHz, MeCN-d_3, RT) of the reaction of Cp*(*exo*-η^4-C_5Me_5H)Co with 4 equivalents of $[Pt(dmpe)_2][PF_6]_2$ illustrating the quantitative hydride transfer to form $[HPt(dmpe)_2][PF_6]_2$. The signal at 1.82 consists of three different peaks, the methyl protons for the hydride product, the methylene protons for the Pt starting material, and also a residual peak from THF. The inset highlights the formation of the hydride peak.

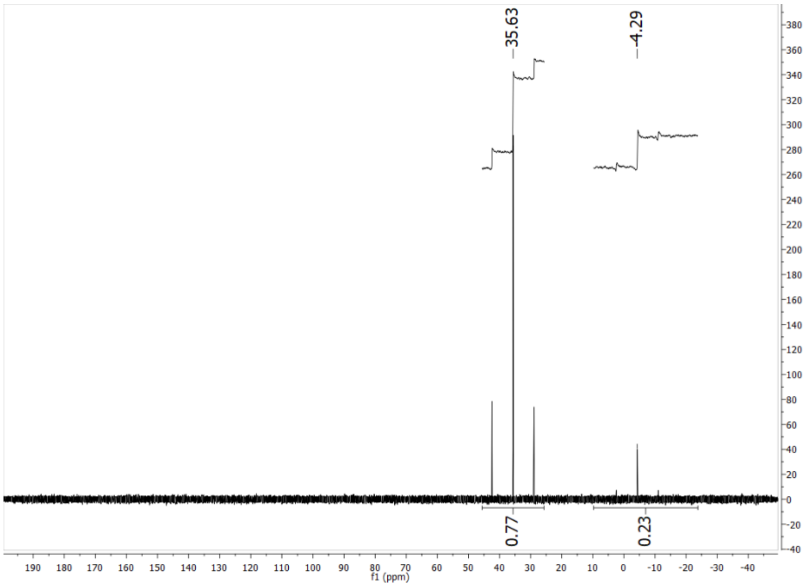

Figure S21: ^{31}P{^{1}H} NMR (162 MHz, MeCN-d_3, RT) of the reaction of Cp*(*exo*-η^4-C_5Me_5H)Co with 4 equivalents of $[Pt(dmpe)_2][PF_6]_2$ illustrating the quantitative hydride transfer to form $[HPt(dmpe)_2][PF_6]_2$.

S.11 Pulse EPR Spectroscopy:

Samples for pulse EPR spectroscopy were prepared as previously described.[21]

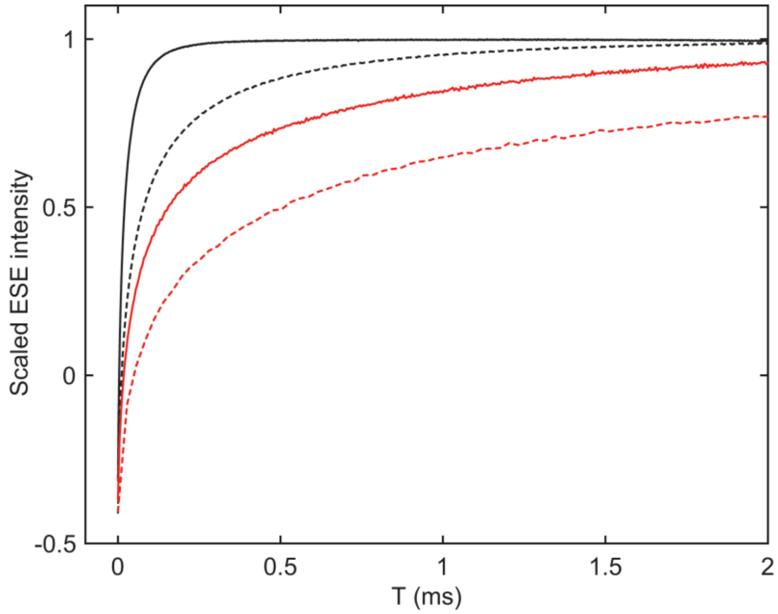

Figure S22: Q-band inversion recovery traces of *endo*- (black) and *exo*-isomers (red) of Cp*$_2$Co protonation acquired at 6 K (dashed lines) and 10 K (solid lines). Data for each species was acquired at the field corresponding to peak spectral intensity for that species. This illustrates the significantly faster relaxation properties of the *endo*-isomer.

Discussion of the Q-band inversion recovery:

Accurate measurement of the T_1' in these species is technically challenging due to their significant **g**-anisotropy. This is because there are contributions to the relaxation from spectral diffusion in addition to explicit spin-lattice relaxation, as only a very small portion of the EPR spectral envelope is acted upon by the initial inversion pulse. Furthermore, the EPR signals of the *exo*-product, overlap with those of the *endo*-product. Thus a multiexponential function would be necessary to model its inversion recovery data and would thus not be well constrained. Nonetheless, a rough estimate of the T_1' can be obtained without fitting of exponential functions by using Equation 5 for the longitudinal magnetization as a function of time in the inversion recovery experiment.

When $M_z = 0$, $T \approx \ln(2) \times T_1'$ (5)

This allows for the following estimates to be made. For the *exo*-species the T_1' is ~80 µs at 6 K and ~25 µs at 10 K. For the *endo*-species the T_1' is ~20 µs at 6 K and ~6 µs at 10 K. This clearly illustrates the significant difference observed in the longitudinal relaxation rates of the two species, which enables relatively clean pulse EPR data (particularly in the case of ENDOR) to be collected.

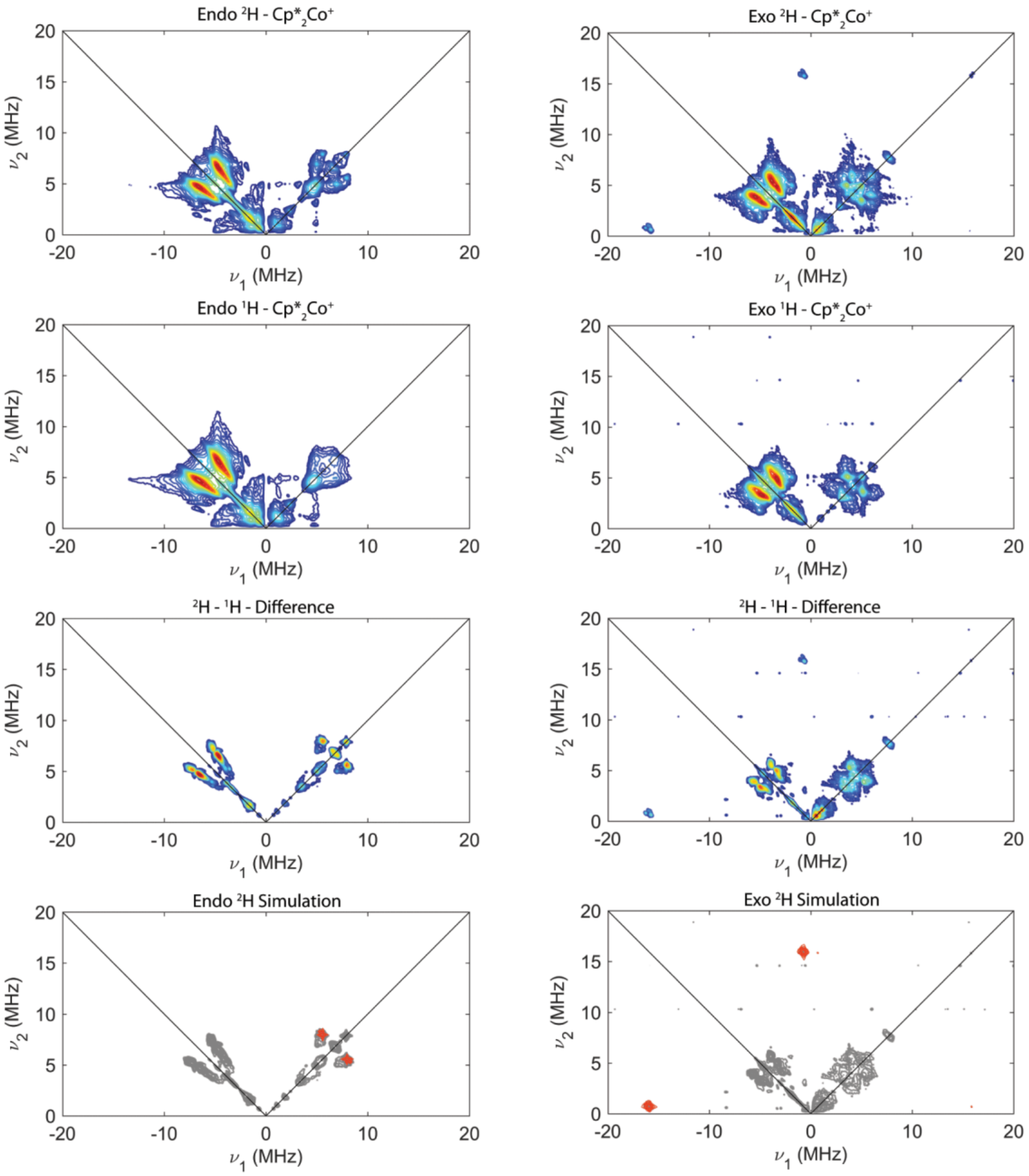

Figure S23: Comparison of Q-band HYSCORE spectra acquired at the center of the EPR spectrum of the Endo (left) and Exo (right) protonated Cp*$_2$Co species generated via reaction with DOTF (top panels) and HOTF (2nd panels from top). To minimize the intensity of the features centered at 5 MHz in the (-,+) quadrant common to both isotopologues, the ^{2}H-^{1}H difference spectrum is shown third from the top. Simulations of the ^{2}H hyperfine couplings derived from the ^{1}H couplings determined via ENDOR for the Endo and Exo species are overlayed in red over the difference spectra, which are plotted in grey. Acquisition parameters: Temperature = 10 K (Endo), 20 K (Exo); Magnetic field = 1038 mT (Endo), 1170 mT (Exo) $\pi/2$ = 12 ns; π = 24 ns; $t_1 = t_2$ = 100 ns, τ = 100 ns; shot repetition time (srt) = 2 ms.

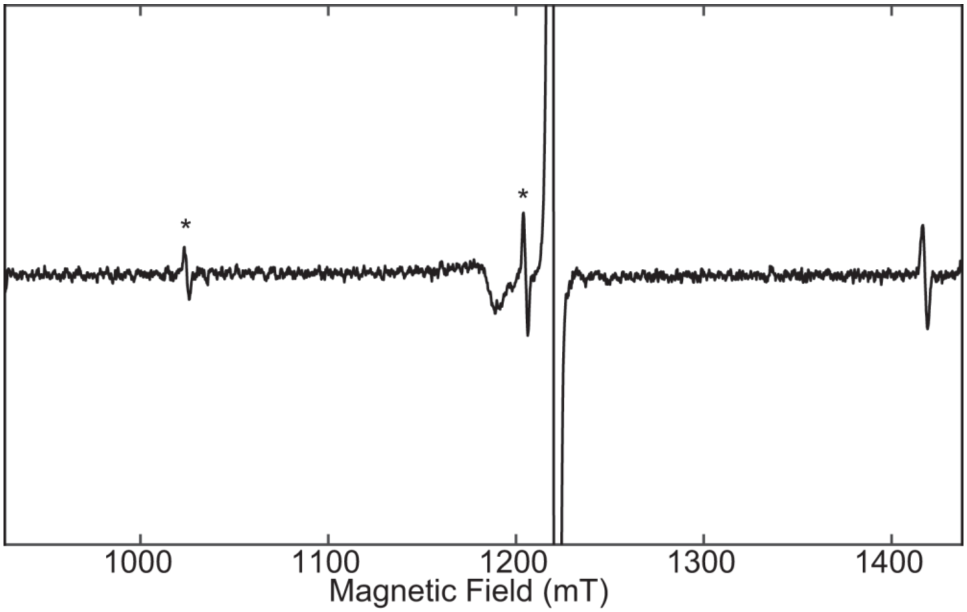

Figure S24: Pseudomodulated Q-band ESE-EPR spectrum at 10 K of a coal standard sample (seen as an intense, isotropic signal at 1200 mT) using the same Bruker Q-band D2 resonator as in this study. There are additionally three sharp signals present in the backround (1025 mT, 1205 mT, and 1418 mT) that arise from a trace paramagnetic species present in a component of the resonator, as well as a broad axial feature from a small amount of Cu(II) at 1184 mT. Two of these sharp background signals, marked with asterisks, are observed in the ESE-EPR spectra acquired at 10 K presented in the main text (Figure 2). The other signal is outside of the measured spectral window in this work. These features are much less intense relative to the signals derived from Cp^*_2Co-protonation at 6 K and thus are not observed in the spectra acquired at that temperature.

Species	g-tensor	$A(^1H)$ (MHz)	$A(^{59}Co)$ (MHz)	e^2qQ/h for Co (MHz)	η
Cp*(*endo*-C_5Me_5H)Co^+	[2.626, 2.349, 1.984]	[19.0, 15.0, 19.5]	[245, 155, 187]	170	<0.1
Cp*(*exo*-C_5Me_5H)Co^+	[2.170, 2.085, 2.005]	[106.5, 112.5, 108.2]	[15, 15, 225]	N.D.	N.D.

Table S1: Simulation parameters derived from the ENDOR, HYSCORE, and CW-EPR spectroscopy.

S.6 CW EPR Spectroscopy

Reaction of Cp^*_2Co with HOTf: These experimental details have been reported previously[21] but are repeated here for convenience. A 1 mL solution of HOTf (23 µL, 3.0 eq) in toluene and a 2 mL solution of Cp^*_2Co (40 mg, 1.0 eq) were chilled to −78 °C for ten minutes in a cold well. With strong stirring of the HOTf solution, the Cp^*_2Co solution was added dropwise over ten minutes. Purple precipitate could be observed upon the addition of each drop. After the completion of the addition, the reaction mixture was allowed to stir for 5 more minutes. The reaction was then vacuum filtered in the cold well through a medium porosity frit to yield a purple solid. This solid was then washed with toluene that had been prechilled to −78 °C (5 mL) and then likewise with prechilled pentane (15 mL). After drying on the frit for ten minutes the solid was then transferred to a prechilled vial. The solid was then dried under vacuum for several hours at −78 °C. This solid was then transferred to an EPR tube and passed out of the glovebox into a dewar filled with liquid nitrogen.

Reaction of Cp*$_2$Co with DOTf: The same experimental protocol as above was used with the exception that DOTf was employed and in all cases where toluene had previously been used it was replaced with toluene-d_8.

Reaction of Cp*$_2$Co with HNTf$_2$: Decamethylcobaltocene (20 mg, 0.061 mmol) was weighed into a 20 mL scintillation vial and dissolved in 5 mL of toluene. Bis(trifluoromethanesulfon)imide (HNTf$_2$) is weighed into a 20 mL scintillation vial and 5 mL of toluene is added and the vial is charged with a stir bar. Both solutions are cooled to −78 °c in the cold well for ten minutes. Then the Cp*$_2$Co solution is added dropwise to the HNTf$_2$ solution while it was being vigorously stirred over five minutes. The reaction mixture is allowed to stir for ten minutes during which it turns purple. Prechilled pentane (10 mL) is added to the toluene solution and the reaction is stirred for another five minutes. The reaction mixture is then filtered through a pre-chilled frit. The solid is then washed with pentane (5 x 2 mL). The solid is then transferred to a pre-chilled vial. The solid is then placed under vacuum for three hours to yield a pale purple solid. This solid is then transferred into a pre-chilled EPR tube and the cold well is then switched to a liquid nitrogen bath. The tube is allowed to cool for ten minutes before it is then quickly transferred out of the box and into a dewar with liquid nitrogen (Figure S24).

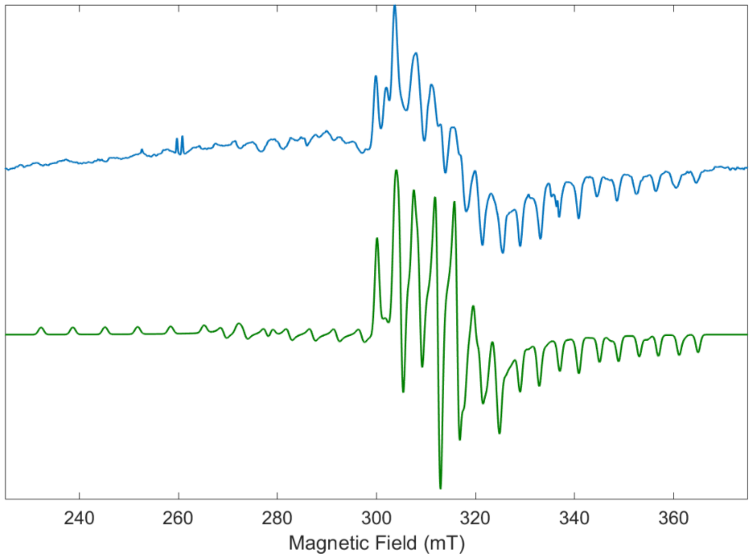

Figure S25: X-Band CW EPR spectrum (blue) at 77 K in the solid state of the precipitate from the reaction of bis(trifluoromethanesulfon)imide) with Cp*$_2$Co at −78 °C in toluene. Simulation (green) of this data using the parameters from Table S1 with a weight of 0.3 on the on the *endo-isomer* and a weight of 1.0 on the *exo*-isomer.

Discussion of Protonation Selectivity:

Both of the protonation reactions are under kinetic control due to the rapid precipitation upon proton transfer. Thus the relative energies of either the transition state or a pre-equilibrium must be affected by the steric bulk of the acid. We believe that this likely due to a hydrogen bonding interaction between the acid and the π-electrons of the Cp* ring. Such hydrogen bonds have previously been observed experimentally by IR and NMR for ferrocene,[32,33] and we have observed computationally the formation of hydrogen bonded interactions between anilinium triflates and Cp*$_2$Co preceding proton transfer.[34] In this model, the thermodynamics of hydrogen bonding for the smaller HOTf reflect those of the isolated products and thus *endo*-protonation is preferred. With the bulkier HNTf$_2$, steric clash with the opposite Cp* ring leads to destabilization of this *endo*-hydrogen bond and thus *exo*-hydrogen bonding and consequently *exo*-protonation is favored.

Oxidation of Cp*(*exo*-η^4-C$_5$Me$_5$H)Co with HBAr^F$_4$: Cp*(*exo*-η^4-C$_5$Me$_5$H)Co (20 mg, 0.061 mmol) was dissolved in pentane and cooled to −78 °C. It was then added to a 50 mL round bottom flask with a large stir bar that was also chilled to −78 °C after it was charged with HBAr^F$_4$ (122.6 mg, 0.12 mmol, 2 equiv.). This was then stirred for several hours during which a pale purple solid was seen to form in the reaction. This can then be filtered through a pre-chilled frit and washed with pre-chilled pentane (5 x 2 mL). The solid was then transferred to a pre-chilled EPR tube. The cold well was then swapped for one that contained liquid nitrogen and the solid was allowed to equilibrate to 77 K. The tube was then quickly passed out of the glovebox into a dewar containing liquid nitrogen. (See Figure S25-26)

Oxidation of Cp*(*exo*-η^4-C$_5$Me$_5$D)Co with HBAr^F$_4$: The same procedure as above was used except now Cp*(*exo*-η^4-C$_5$Me$_5$D)Co was used. (See Figure S50-51)

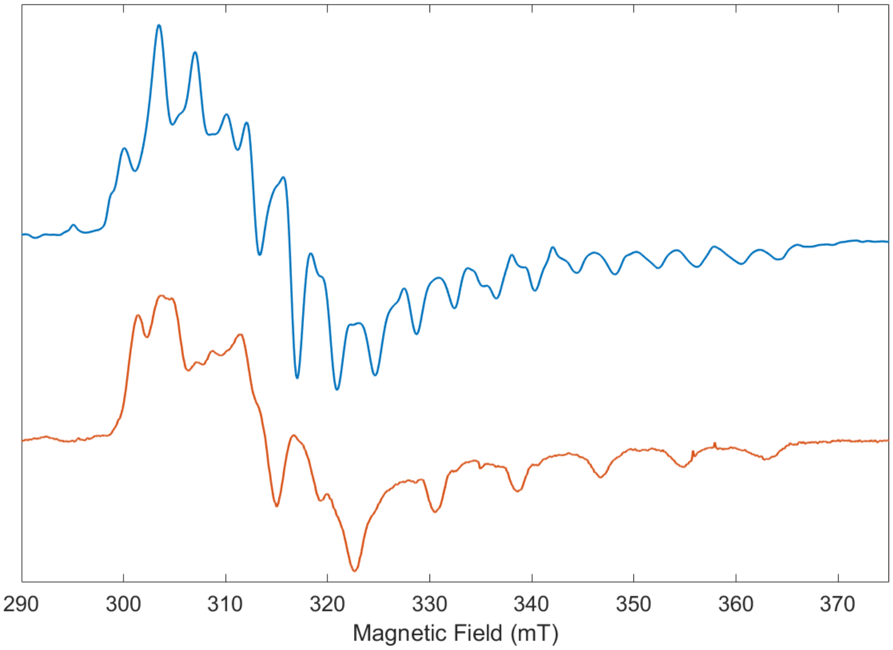

Figure S26: A comparison of the 77 K, X-band EPR spectra of solid samples of [Cp*(*exo*-η^4-C$_5$Me$_5$H)Co][BArF] (blue) and [Cp*(*exo*-η^4-C$_5$Me$_5$D)Co][BArF] (orange).

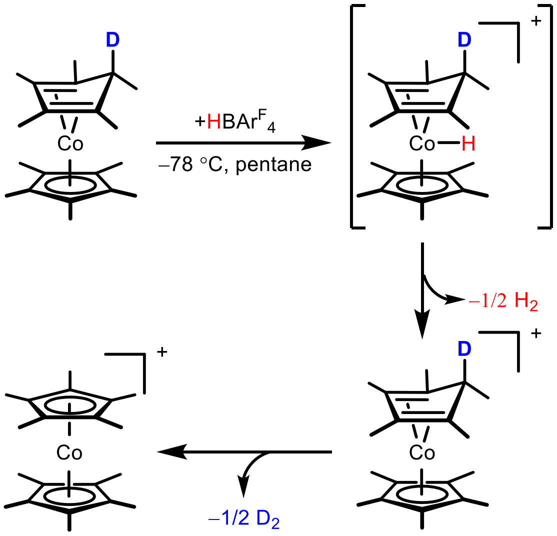

Figure S27: A depiction of our mechanistic proposal to account for observations upon the reaction of Cp*(*exo*-C_5Me_5D)Co with $HBAr^F_4$. Efforts to identify the bracketed Co^{III}–H intermediate at low temperature using NMR spectroscopy always resulted in the sole observation of the terminal oxidation product $Cp^*_2Co^+$. However, we believe that formation of this species is reasonable on the basis of DFT which suggests that the most favorable site of protonation (*endo*, *exo*, or Co) is the Co (see Table S5). This proposal is supported by the known protonation of 18e⁻ Cp-Co^I species to form hydrides.[35,36] DFT calculations suggest that this Co–H bond is homolytically weak ($BDFE_{Co-H}$ = 51 kcal mol^{-1}). Thus it should be able to react with itself or with the starting material to release H_2 or HD bimolecularly and form the experimentally observed product, Cp*(*exo*-C_5Me_5D)Co^+. It is quite possible that the precipitated solid is contaminated with the Co^{III}–H species, which we would also expect to be fairly insoluble under the reaction conditions, but due to the expected diamagnetic nature of this species we would not observe it by EPR techniques.

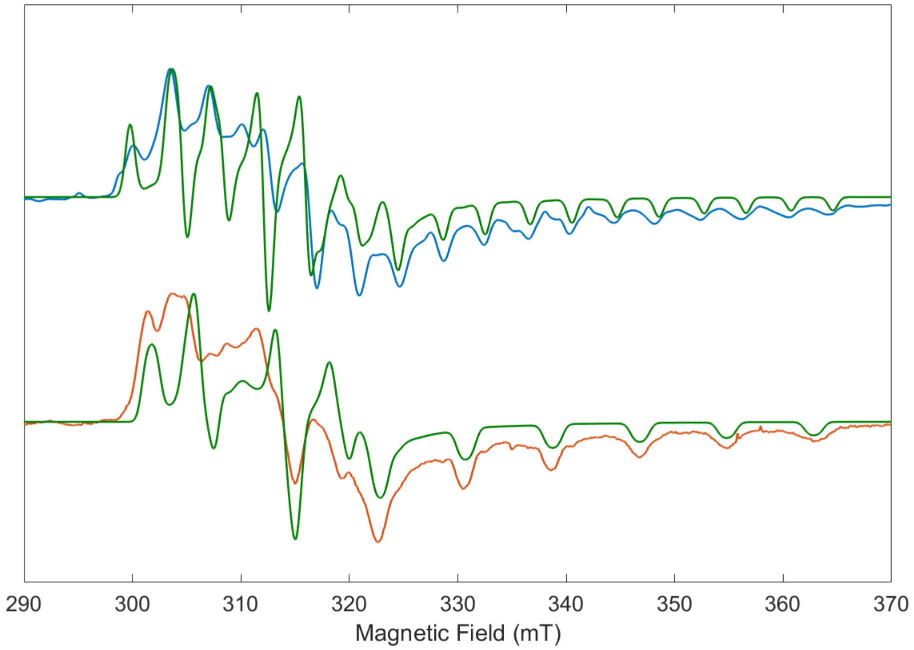

Figure S28: A comparison of the data to the simulation (green) for the 77 K, X-band EPR spectra of solid samples of [Cp*(*exo*-η^4-C_5Me_5H)Co][BArF] (blue) and [Cp*(*exo*-η^4-C_5Me_5D)Co][BArF] (orange). Simulation parameters are the same in both cases (Table S1) except for $A(^1H)$ being scaled down by the ratio of the gyromagnetic ratio for proton:deuterium (~6.5) in the simulation for [Cp*(*exo*-η^4-C_5Me_5D)Co][BArF] (bottom). We believe that the small deviation of the observed EPR spectra from the simulations can be accounted for by the fact that there is likely a significant difference in hydrogen bonding with the $BAr^F{}_4{}^-$ counteranion as compared to the OTf^- counteranion for which the simulation parameters were derived using pulse EPR.

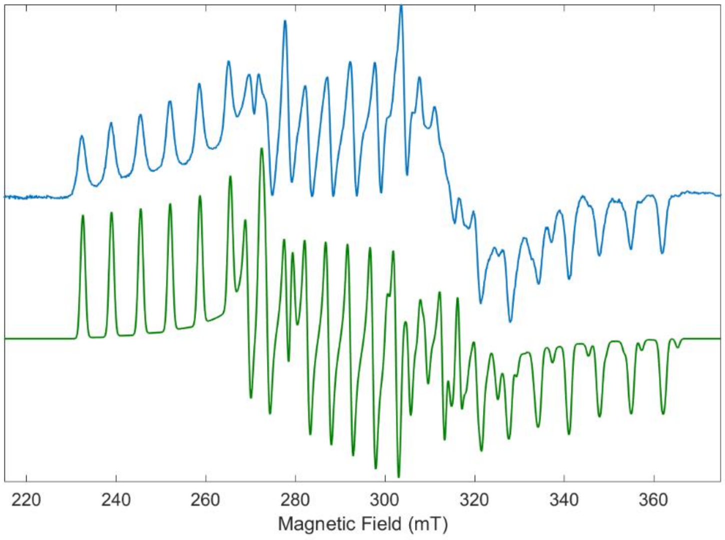

Figure S29: X-Band CW EPR spectrum (blue) at 77 K in the solid state of the precipitate from the reaction of trifluoromethanesulfonic acid with $Cp^*{}_2Co$ at −78 °C in toluene.[21] Simulation (green) of this data using the parameters from Table S1 with a weight of 1.0 on the species measured at 6 K (endo) and a weight of 0.1 on the species measured at 10 K (exo).

S7. Electrochemistry

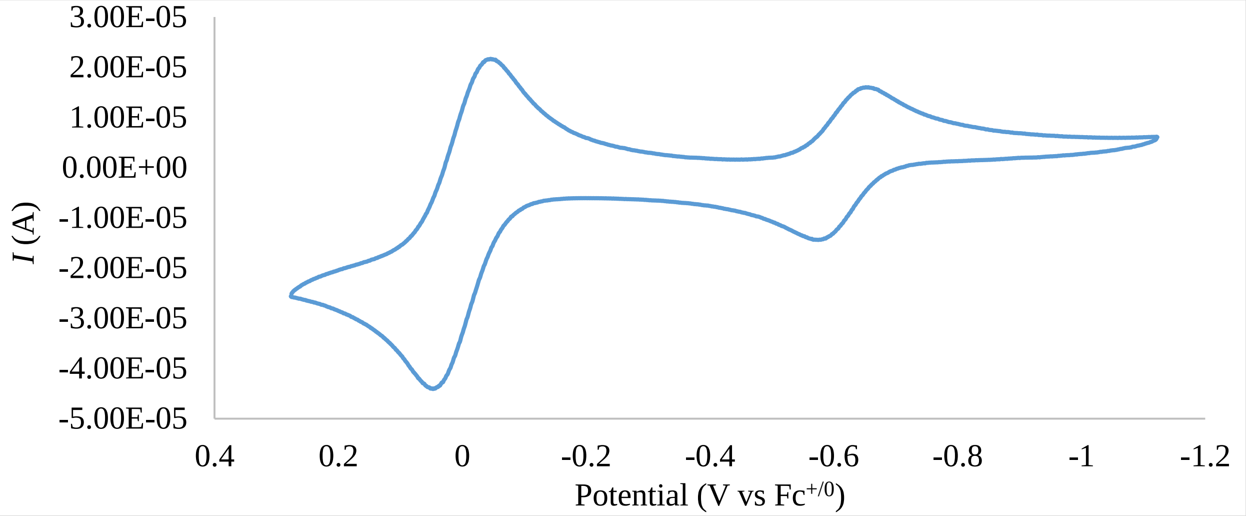

Figure S30: Cyclic voltammogram of Cp*(η^4-C_5Me_6)Co at room temperature in an acetonitrile solution of 0.2 M [TBA][PF_6] with ferrocene added as an internal reference. From this a potential of −0.61 V is determined for the Cp*(η^4-C_5Me_6)$Co^{0/+}$ couple. This potential is shifted by ~0.05 V from that previously reported in DCM (−0.21 V vs SCE in DCM and −0.16 V vs SCE in DME.[37] This small shift is attributed to going to the more coordinating acetonitrile solvent.

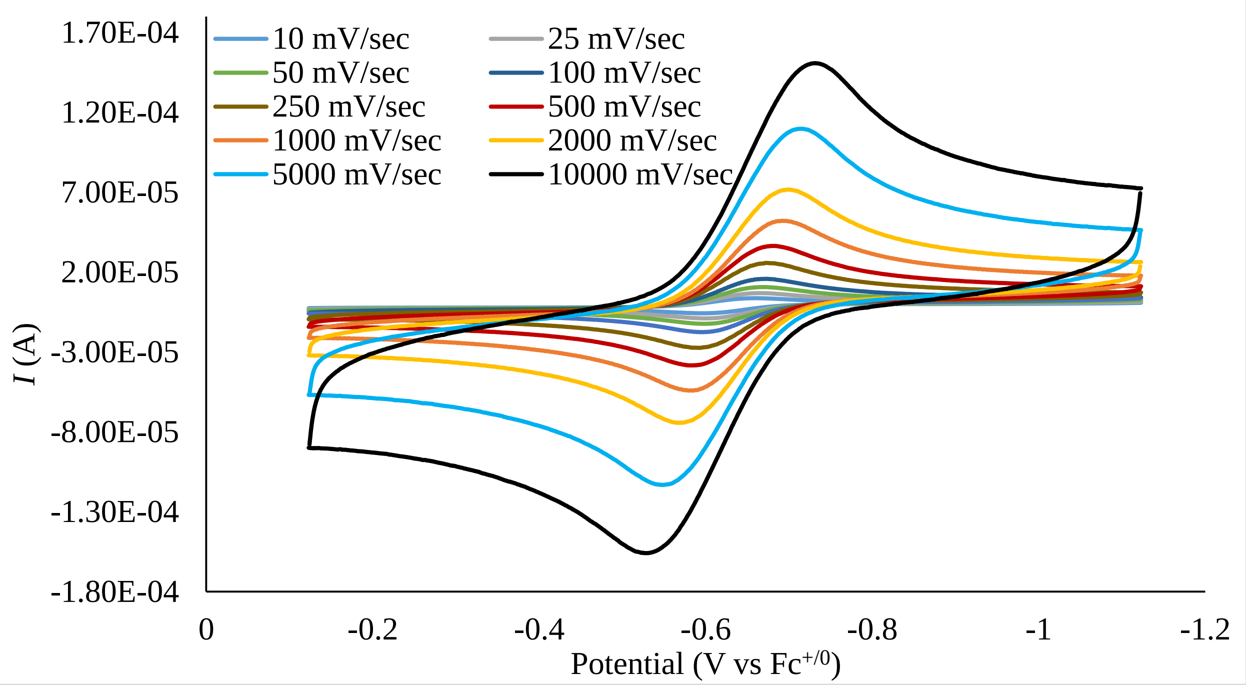

Figure S31: Scan rate dependence of the Cp*(η^4-C_5Me_6)$Co^{+/0}$ at room temperature in an acetonitrile solution of 0.2 M [TBA][PF_6]. This demonstrates the high reversibility of this couple in contrast to what is observed with Cp*(*exo*-η^4-C_5Me_5H)Co

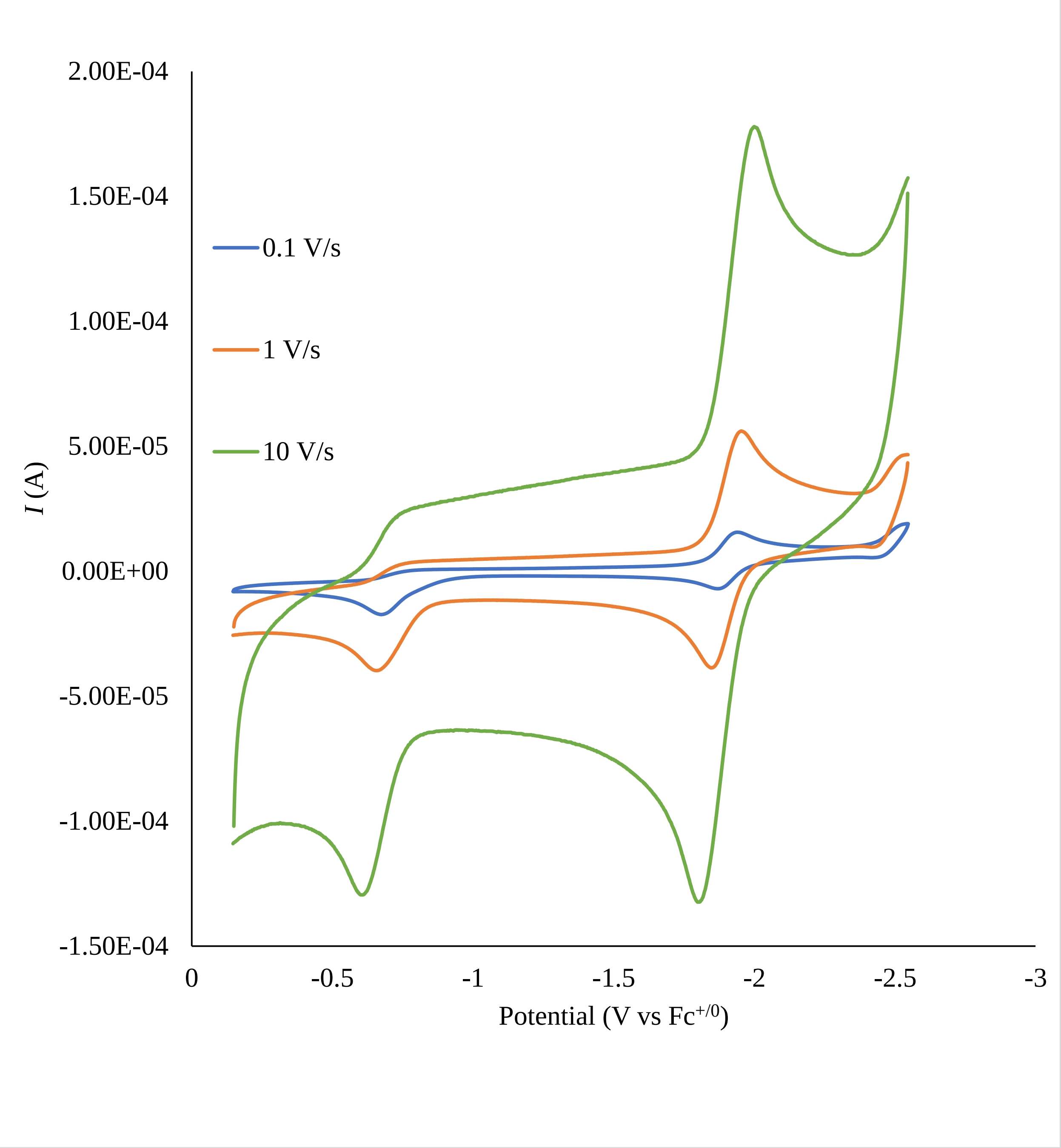

Figure S32: Cyclic voltammograms of Cp*(*exo*-η^4-C_5Me_5H)Co at room temperature at different scan rates in a butyronitrile solution of 0.4 M [TBA][PF_6]. The quasi-reversible oxidation event at ~−0.6 V corresponds to the Cp*(*exo*-η^4-C_5Me_5H)Co$^{0/+}$ couple while the highly reversible redox couple at ~−1.9 V corresponds to the known Cp*$_2$Co$^{0/+}$ couple observed due to decomposition of Cp*(*exo*-η^4-C_5Me_5H)Co$^+$ to form Cp*$_2$Co$^+$. There is the onset of another apparently irreversible reduction event apparent at even more negative potentials. Although this was not explored thoroughly it is in agreement with reports on Cp(η^4-C_5H_5R)Co complexes (R = alkyl or H) which were found to undergo an irreversible reduction at negative potentials.[38]

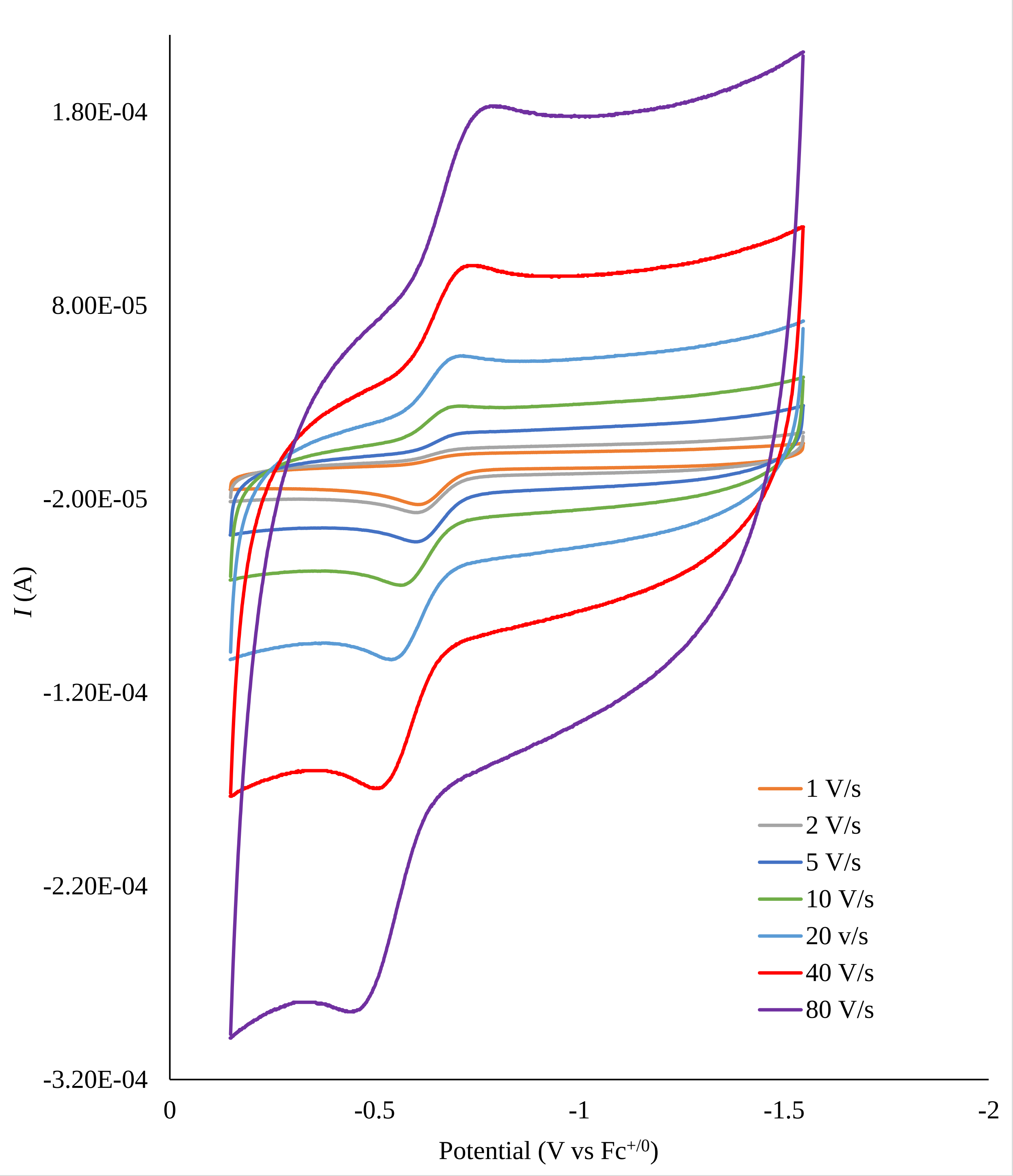

Figure S33: Cyclic voltammograms of Cp*(*exo*-η^4-C_5Me_5H)Co at room temperature at different scan rates in a butyronitrile solution of 0.4 M [TBA][PF_6]. These demonstrate the increasing reversibility of the couple at extremely high scan rates (maximum i_c/i_a ~0.62). From the highest scan rate we are able to determine an oxidation potential for Cp*(*exo*-η^4-C_5Me_5H)Co of −0.62 V in good agreement with that observed for Cp*(η^4-C_5Me_6)Co.

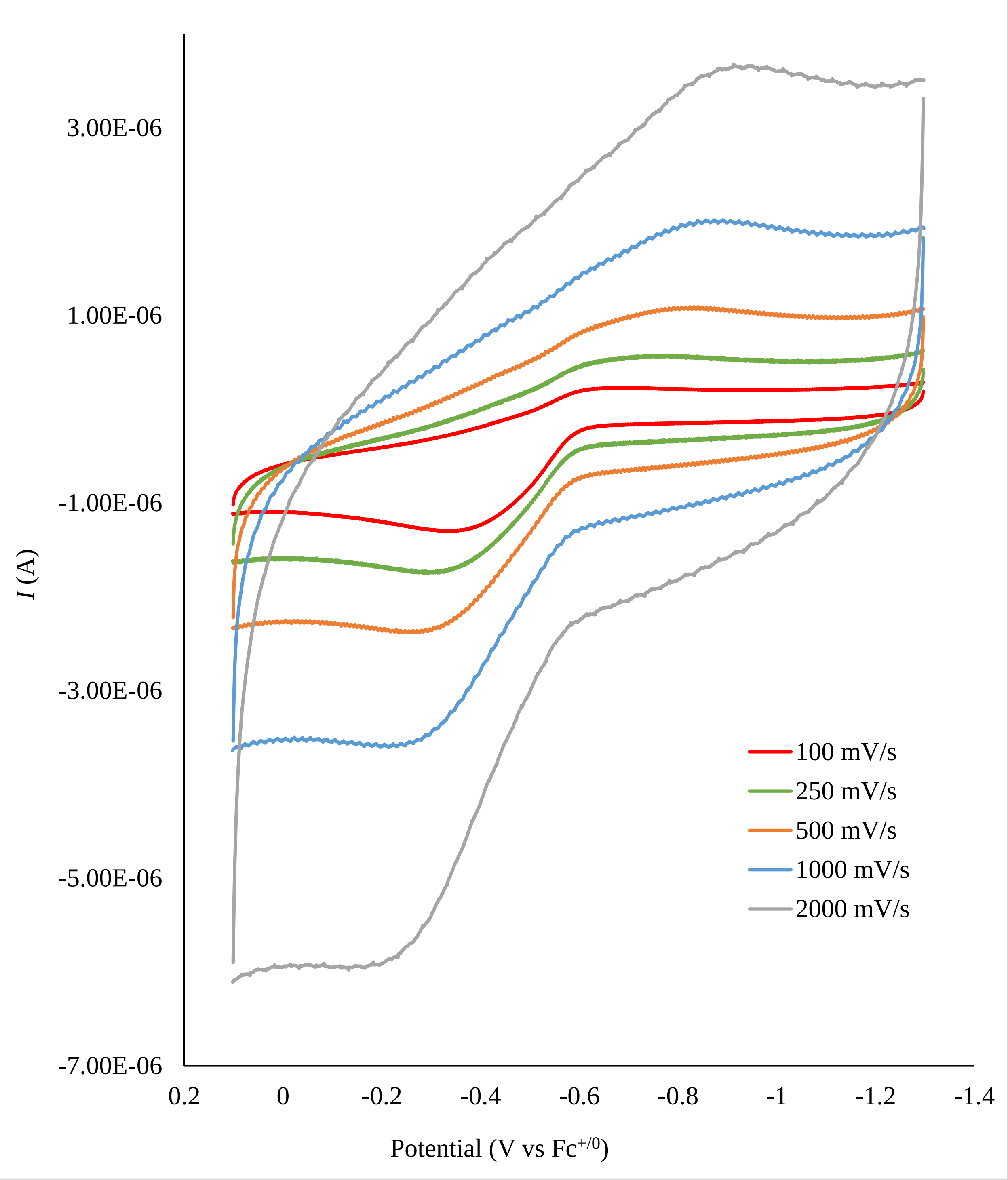

Figure S34: Cyclic voltammograms of Cp*(*exo*-η^4-C_5Me_5H)Co at room temperature at different scan rates in a butyronitrile solution of 0.4 M [TBA][PF_6]. We can see that a degree of reversibility is achieved at lower scan rates than are necessary at room temperature. A comparison is shown in Figure S15. Attempts to go to the higher scan rates that were used at room temperature were not successful likely due to the increased resistivity at low temperature.

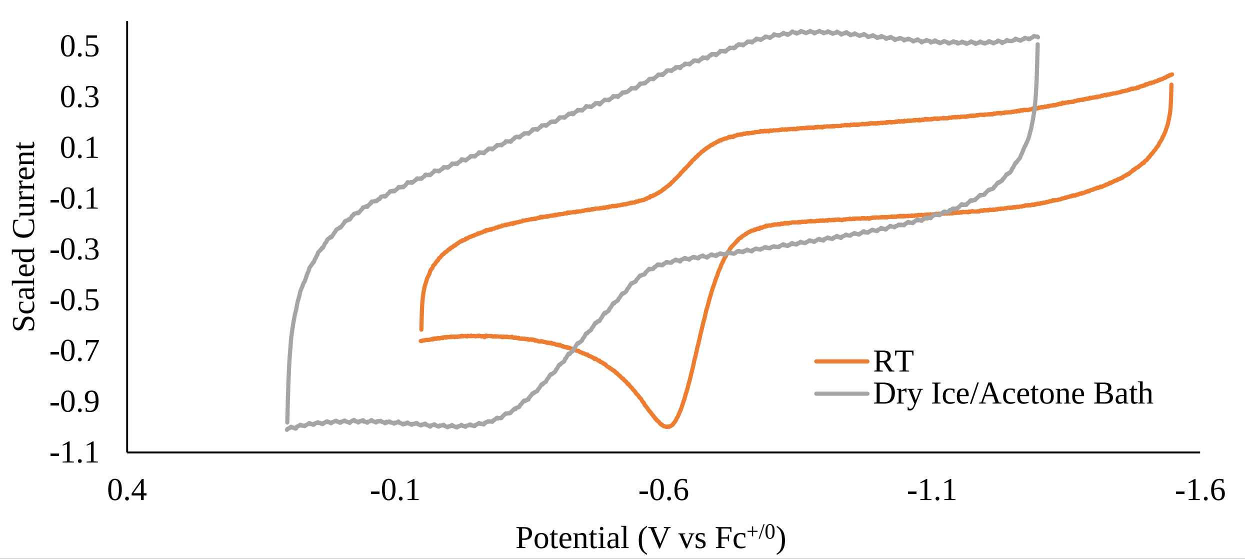

Figure S35: Comparison of cyclic voltammograms taken at room temperature (~22 °C) and after cooling the electrochemical cell immersed in a dry ice/acetone bath (−78 °C). Both voltammograms are taken at a scan rate of 1 V/s with a concentration of analyte of 1 mM and 0.4 M [TBA][PF_6] in butyronitrile. This demonstrates that cooling the cell leads to a significant enhancement of reversibility at a particular scan rate. In order to facilitate the comparison each of the currents have been scaled by dividing them by the absolute value of the peak cathodic current. It is apparent here that the redox couple appears to drift to a slightly more positive potential of −0.56 V when measured at −78 °C. This drift in potential is not uncommon and only represents a ΔBDFE = 23.06 × 0.05 = 1.4 kcal mol^{-1}. We have used the potential measured at room temperature in our thermodynamic calculations in the main text as that represents the standard state.

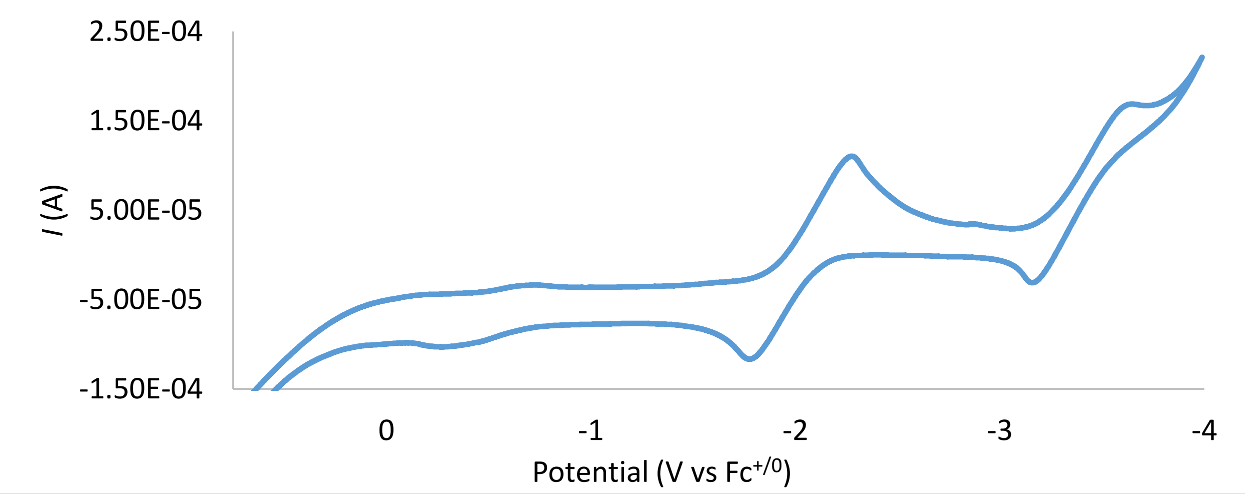

Figure S36: Cyclic voltammograms of Cp^*_2Co at room temperature in 0.1 M [TBA][PF_6] dissolved in THF. The spectrum is referenced to the Cp^*_2Co reduction potential in MeCN of −1.96 V as a reference. After scanning through the reduction of Cp^*_2Co you can then observe the irreversible feature at ~−0.6 V associated with $Cp^*(\eta^4\text{-}C_5Me_5H)Co^{0/+}$. This suggests that there is a small amount of available proton source, likely water.

S.8 X-ray Crystallography Data:

Compound	*exo*-Cp*(η^4-C_5Me_5H)Co	Cp*(C_5Me_6)Co
Chemical Formula	$C_{20}H_{31}Co$	$C_{21}H_{33}Co$
Formula Weight	330.38	344.43
Crystal System	Monoclinic	Monoclinic
Space Group	$P2_1/n$	$P2_1/c$
a [Å]	8.0700(6)	12.8973(5)
b [Å]	8.4605(6)	9.6767(4)
c [Å]	12.8684(10)	15.1146(6)
α [°]	90	90
β [°]	93.611(2)	92.956(2)
γ [°]	90	90
V [$Å^3$]	876.86(11)	1883.84(13)
Z	2	4
D_{calcd} [g cm^{-1}]	1.251	1.214
F_{000}	356.0	984.0
μ [mm^{-1}]	0.971	0.93
Temperature [K]	100(2)	100(2)
Wavelength [Å]	0.71073	0.71073
Measured Reflections	38760	117581
Unique Reflections	5620	8739
Data/Restraints/Parameters	5620/0/115	8739/0/210
R(F) (I>2σ(I))	0.0382	0.0471
wR(F^2) (all)	0.0838	0.0897
GOOF	1.016	1.045

Table S2: Crystallographic details for *exo*-Cp*(η^4-C_5Me_5H)Co and Cp*(η^4-C_5Me_6)Co.

S.9 IR Spectroscopy

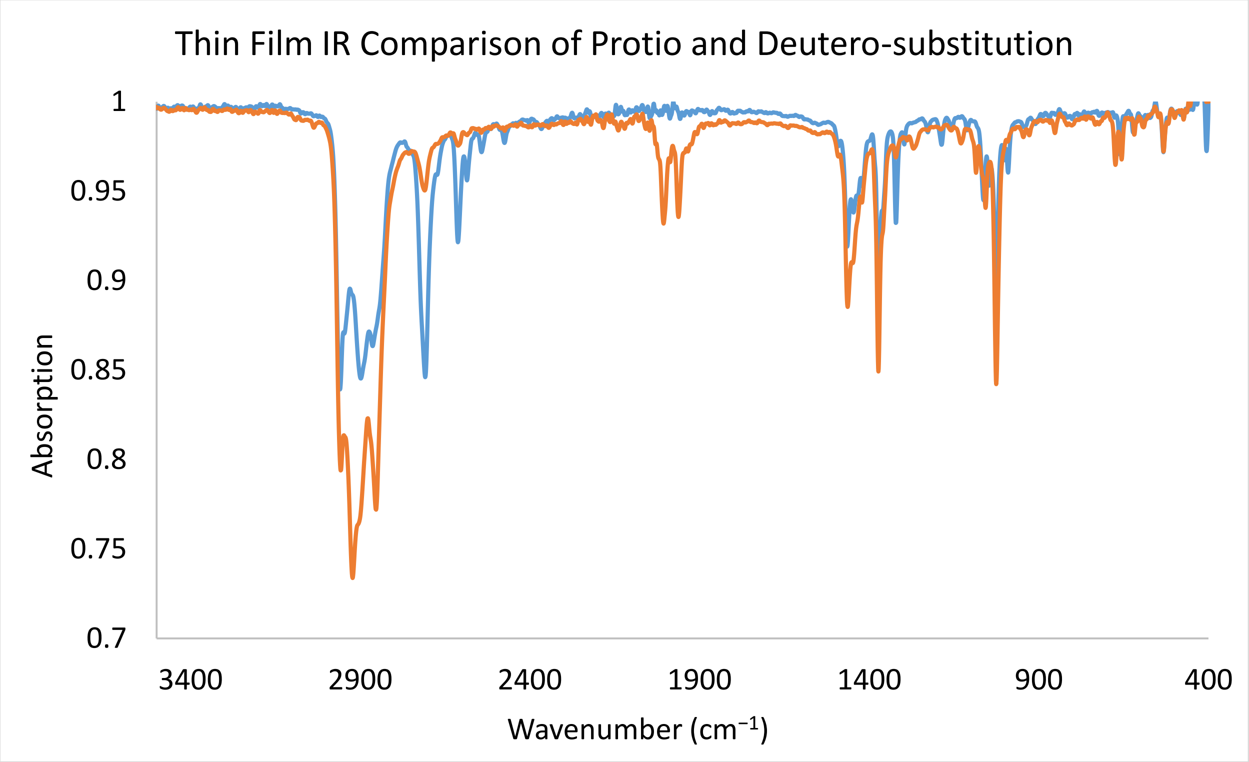

Figure S37: Thin film IR spectra of Cp*(*exo*-η^4-C_5Me_5H)Co (blue) and Cp*(*exo*-η^4-C_5Me_5D)Co (orange). C–H vibrations at 2708 cm^{-1} and 2612 cm^{-1} shift to 2005 cm^{-1} and 1962 cm^{-1}. The predicted shift for deuterium substitution based on a simple harmonic oscillator model would be to 1987 cm^{-1} and 1917 cm^{-1}.

It is unclear why there are two stretches visible for this C–H/D mode. It is clear from solution NMR studies that these molecules consist of only one regioisomer (*exo* with no *endo*- contamination) but this phenomenon persists in the solution IR (Figure S37). Similar behavior was observed for Cp(η^4-C_5H_6)Co and Cp(*exo*-η^4-C_5H_5D)Co by Wilkinson and no regioisomerism is possible in that molecule.[39] We have not found other examples of Cp−H or Cp*−H species in the literature that have been characterized by IR spectroscopy. We suggest that the different stretches arise from conformational isomers relating to the eclipsed or staggered nature of the ring that are causing the different stretching frequencies. This has been observed before for Cp* species of M−H.[40]

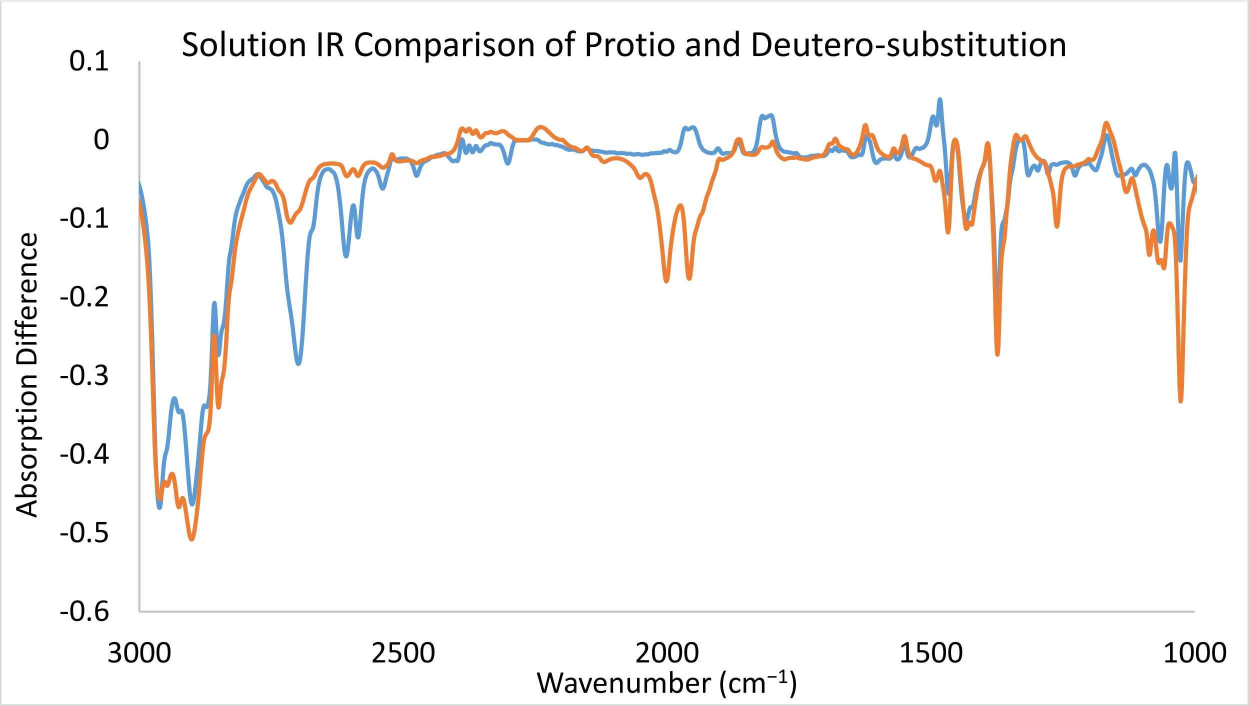

Figure S38: Solution state IR spectra of Cp*(*exo*-η^4-C_5Me_5H)Co (blue) and Cp*(*exo*-η^4-C_5Me_5D)Co (orange) in C_6D_6. This spectra demonstrates the same behavior as the thin film IR does demonstrating that the observed behavior is not only a solid state phenomenon.

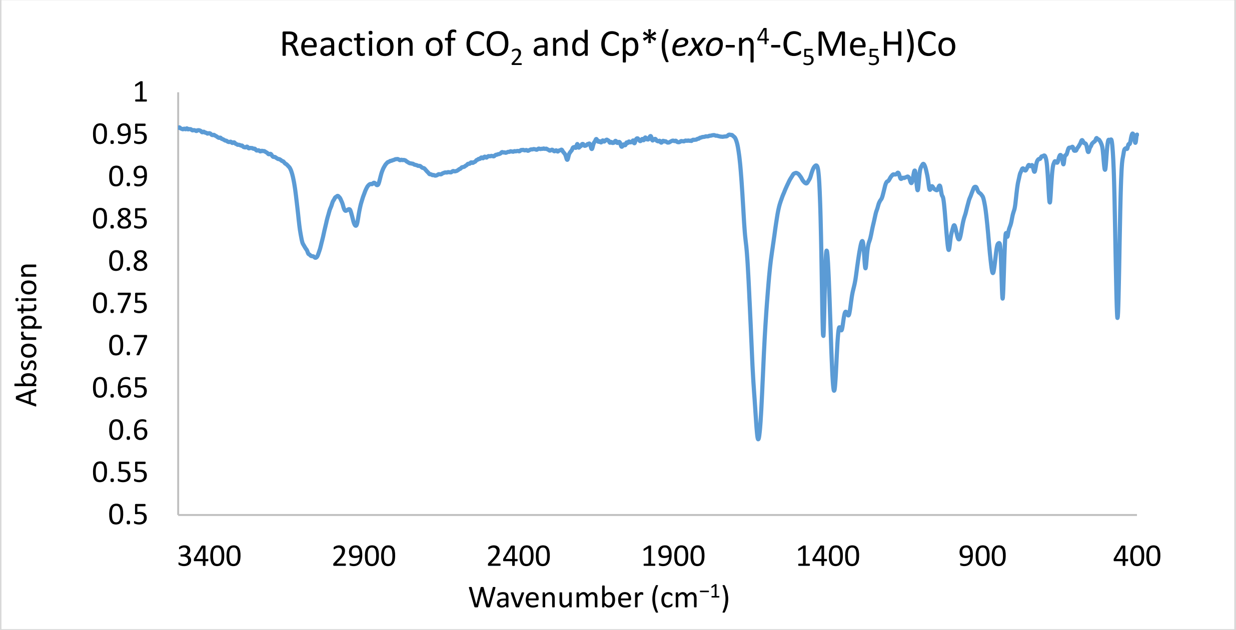

Figure S39: Thin film IR spectrum of the reaction between Cp*(*exo*-η^4-C_5Me_5H)Co and CO_2 demonstrating the formation of [Cp^*_2Co][HCO_2]. The features demonstrated here are similar to those previously characterized for tetramethylammonium formate.[41] In particular the unusually low C–H stretch (2666 cm^{-1}) and the C=O (1626 cm^{-1}) stretch are diagnostic for this species.

S.10 Thermochemistry:

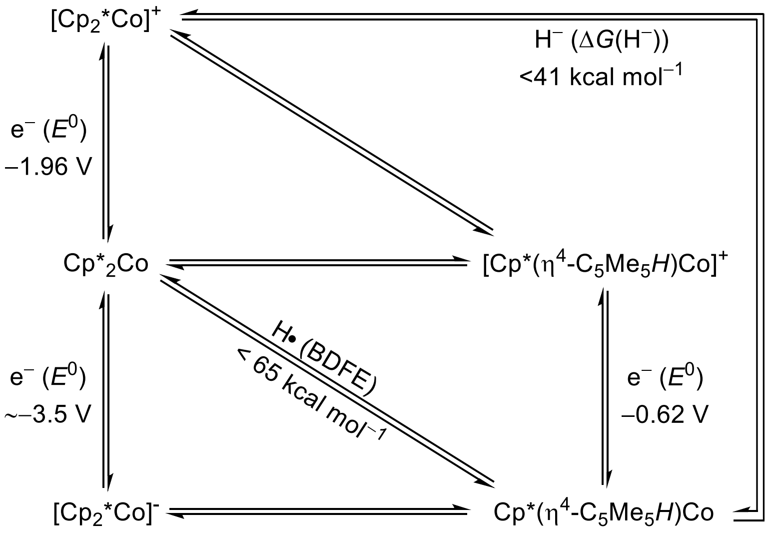

Figure S40: Measured thermochemical parameters.

BDFE $[Cp^*(\textit{exo}\text{-}\eta^4\text{-}C_5Me_5H)Co]^+ \longrightarrow [Cp^*_2Co]^+ + H\bullet$

$-E° = 0.62$ V vs $Fc^{+/0}$ $[Cp^*(\textit{exo}\text{-}\eta^4\text{-}C_5Me_5H)Co]^+ + e^- \longrightarrow Cp^*(\textit{exo}\text{-}\eta^4\text{-}C_5Me_5H)Co$

$\Delta G(H^-) < 41\ \text{kcal mol}^{-1}$ $Cp^*(\textit{exo}\text{-}\eta^4\text{-}C_5Me_5H)Co \longrightarrow [Cp^*_2Co]^+ + H^-$

$\Delta G° = -26\ \text{kcal mol}^{-1}$ $H^- \longrightarrow H\bullet + e^-$

$$\text{BDFE} < 23.06 \times -E° + \Delta G(H^-) + \Delta G°$$

$$\text{BDFE} < 23.06 \times 0.62 + 41 - 26$$

$$\text{BDFE} < 29\ \text{kcal mol}^{-1}$$

Figure S41: Describes the process of determining the C–H BDFE in $[Cp^*(\textit{exo}\text{-}\eta^4\text{-}C_5Me_5H)Co]^+$ using the measured hydricity of $Cp^*(\textit{exo}\text{-}\eta^4\text{-}C_5Me_5H)Co$ and the redox potential of $Cp^*(\textit{exo}\text{-}\eta^4\text{-}C_5Me_5H)Co$. There is some disagreement over the hydricity of $[HPt(dmpe)_2][PF_6]$ in the literature so we have chosen to use the more conservative value of $\Delta G(H^-) = 41\ \text{kcal mol}^{-1}$.[42,43]

$$\text{BDFE} \qquad [\text{Cp*}(exo\text{-}\eta^4\text{-C}_5\text{Me}_5\text{H})\text{Co}]^+ \longrightarrow [\text{Cp*}_2\text{Co}]^+ + \text{H}\bullet$$

$$-E°_1 = 0.61 \text{ V vs Fc}^{+/0} \qquad [\text{Cp*}(exo\text{-}\eta^4\text{-C}_5\text{Me}_5\text{H})\text{Co}]^+ + \text{e}^- \longrightarrow \text{Cp*}(exo\text{-}\eta^4\text{-C}_5\text{Me}_5\text{H})\text{Co}$$

$$\text{BDFE} < 65 \text{ kcal mol}^{-1} \qquad \text{Cp*}(exo\text{-}\eta^4\text{-C}_5\text{Me}_5\text{H})\text{Co} \longrightarrow \text{Cp*}_2\text{Co} + \text{H}\bullet$$

$$E°_2 = -1.96 \text{ V vs Fc}^{+/0} \qquad \text{Cp*}_2\text{Co} \longrightarrow [\text{Cp*}_2\text{Co}]^+ + \text{e}^-$$

$$\text{BDFE} < 23.06 \times -E°_1 + \text{BDFE} + 23.06 \times E°_2$$

$$\text{BDFE} < 23.06 \times 0.61 + 65 + 23.06 \times -1.96$$

$$\text{BDFE} < 34 \text{ kcal mol}^{-1}$$

Figure S42: Describes the process of determining the C–H BDFE in [Cp*(*exo*-η^4-C_5Me_5H)Co]$^+$ using the measured BDFE C–H of Cp*(*exo*-η^4-C_5Me_5H)Co and the redox potential of Cp*(*exo*-η^4-C_5Me_5H)Co and $Cp*_2Co$.

S.11 DFT Calculations:

Functional for Optimization	Species	Spin State	Absolute Energy (Hartrees)	Relative Energy (kcal mol^{-1})
TPSSH	Co–H	$S = 1/2$	−2162.647	18.42
TPSSH	*endo*-C–H	$S = 1/2$	−2162.676	0
TPSSH	*exo*-C–H	$S = 1/2$	−2162.673	1.82
BP86	Co–H	$S = 1/2$	−2162.773	16.93
BP86	*endo*-C–H	$S = 1/2$	−2162.800	0
BP86	*exo*-C–H	$S = 1/2$	−2162.796	2.10
B3LYP	Co–H	$S = 1/2$	−2161.879	20.91
B3LYP	*endo*-C–H	$S = 1/2$	−2161.913	0
B3LYP	*exo*-C–H	$S = 1/2$	−2161.911	1.02
TPSS	Co–H	$S = 1/2$	−2162.785	15.72
TPSS	Co–H	$S = 3/2$	−2162.725	46.73
TPSS	*endo*-C–H	$S = 1/2$	−2162.810	0
TPSS	*endo*-C–H	$S = 3/2$	−2162.746	33.61
TPSS	*exo*-C–H	$S = 1/2$	−2162.809	0.51
TPSS	*exo*-C–H	$S = 3/2$	−2162.744	34.92

Table S3: Thermochemistry for the structures optimized with different functionals. In the B3LYP, TPSSH, and BP86 structures the Co–H has a small negative frequency which could affect the relative energies but given the magnitude likely would not affect the relative ordering.

Species	Spin State	Absolute Energy (Hartrees)	Relative Energy (kcal mol^{-1})
Cp*(*exo*-η^4-C_5Me_5H)Co	$S = 0$	−2162.995	0
Cp*(*exo*-η^4-C_5Me_5H)Co	$S = 1$	−2162.954	26.18
Cp*(*endo*-η^4-C_5Me_5H)Co	$S = 0$	−2162.995	0.22
Cp*(*endo*-η^4-C_5Me_5H)Co	$S = 1$	−2162.955	25.29
$Cp^*_2Co–H$	$S = 0$	−2162.940	34.44
$Cp^*_2Co–H$	$S = 1$	−2162.940	34.46

Table S4: Thermochemistry for the different potential isomers of neutral, H-functionalized species. Note that both of the Co–H structures have small imaginary frequencies (~−80 cm^{-1}) indicating that they may be transition states representing transfer of the hydride between the two rings but they have been included here for completeness.

Species	Spin State	Absolute Energy (Hartrees)	Relative Energy (kcal mol^{-1})
[Cp*(*exo*-η^4-C_5Me_5H)Co–H]$^+$	$S = 0$	-2163.381	0
[Cp*(*exo*-η^4-C_5Me_5H)Co–H]$^+$	$S = 1$	-2163.354	17.34
[(*exo*-η^4-C_5Me_5H)Co (*endo*-η^4-C_5Me_5H)Co]$^+$	$S = 0$	-2163.358	14.38
[(*exo*-η^4-C_5Me_5H)Co (*endo*-η^4-C_5Me_5H)Co]$^+$	$S = 1$	-2163.342	24.60
[(*exo*-η^4-C_5Me_5H)Co (*exo*-η^4-C_5Me_5H)Co]$^+$	$S = 0$	-2163.357	15.18
[(*exo*-η^4-C_5Me_5H)Co (*exo*-η^4-C_5Me_5H)Co]$^+$	$S = 1$	-2163.340	26.12

Table S5: Thermochemistry for the different potential isomers resulting from the protonation of Cp*(*exo*-η^4-C_5Me_5H)Co.

Methods for Determining Thermochemical Parameters via DFT: See above under general procedures for information on how the calculations were performed.

BDFE's: To determine the DFT-predicted gas-phase BDFE's (Main Text Figure 1) we followed a protocol that we have published previously.[44] In this protocol, the ΔG for a series of small molecules with known gas-phase BDFE's are calculated ($\Delta G = (G(X\bullet) + G(H\bullet)) - G(X–H)$). A correlation between ΔG and the BDFE is then established ($BDFE = 0.996 \times \Delta G + 4.376$). This allows for accurate gas-phase BDFE's to be calculated. Because of the large differences between how acetonitrile solvation effects X–H bond strengths[45] no efforts have been made to calculate solution state BDFE values but it can be anticipated that they would be stronger (5-10 kcal mol^{-1}) than those in the gas phase with larger errors being encountered for more acidic species in which H-bonding plays a more noticeable role.

Redox Potentials: Ferrocene and ferrocenium were optimized using the same input parameters used for all of the thermochemical calculations. By creating a square scheme and taking the known $Fc^{+/0}$ couple as 0 V we were then able to determine the DFT-predicted redox potential. The energies used in this case were after the solvation correction as described in the general methods.

pK_a: To determine the gas-phase pK_a we again used a square scheme by calculating the ΔG for a conjugate acid/base pair with a known pK_a in acetonitrile. All calculated ΔG values could then be referenced using this to generate an absolute pK_a value. We chose aniline and anilinium as our pair due to its catalytic relevance. The energies used in this case were after the solvation correction as described in the general methods.

Hydricity: To determine the solution-phase hydricity we again used a square scheme by calculating the ΔG for a hydride donor/acceptor pair with a known hydricity in acetonitrile. In this case we chose CO_2 and formate given their relevance to this report. Based on the ΔG of this reaction, we then determined the hydricity of the desired compound. The energies used in this case were after the solvation correction as described in the general methods.

Species	Energy (Hartrees)
$Cp^*_2Co^-$ ($S = 0$)	−2162.408
$Cp^*_2Co^-$ ($S = 1$)	−2162.384
Cp^*_2Co	−2162.409
$Cp^*_2Co^+$	−2162.258
Cp*(η^4-$C_5Me_4CH_2$)Co	−2161.81
Cp_2Fe	−1650.623
Cp_2Fe^+	−1650.37969
Aniline	−287.363
Anilinium	−287.714
CO_2	−188.484
Formate	−189.069
H•	−319.972
$Cp^*_2Ni^+$	−2287.758
$Cp^*_2Ni^{2+}$	−2287.426
Cp*(*exo*-η^4-C_5Me_5H)Ni$^+$	−2288.343
Cp*(*exo*-η^4-C_5Me_5H)Ni^{2+}	−2287.977

Table S6: Gas phase Gibbs Free Energies for species necessary for determining the thermochemical parameters.

Species	BDFE (kcal mol^{-1})	Oxidation Potential (V vs Fc$^{+/0}$)	Hydricity (kcal mol^{-1})	pK_a
$Cp^*_2Co^-$	N/A	−3.28	N/A	N/A
Cp^*_2Co	62.4	−2.16	N/A	N/A
Cp*(*exo*-η^4-C_5Me_5H)Co	52.6	−0.88	37	49.8
Cp*(*endo*-η^4-C_5Me_5H)Co	52.3	−0.98	37	49.6
Cp^*_2Co–H	7.3	−1.63	4	25.2
Cp*(*exo*-η^4-C_5Me_5H)Co$^+$	22.1	N/A	N/A	9.3
Cp*(*endo*-η^4-C_5Me_5H)Co$^+$	24.2	N/A	N/A	10.8
Cp^*_2Co–H$^+$	18.3	N/A	N/A	−2.6
Cp*(*exo*-η^4-C_5Me_5H)Ni$^+$	51.4	N/A	N/A	N/A
Cp*(*exo*-η^4-C_5Me_5H)Ni^{2+}	30.1	N/A	N/A	N/A

Table S7: Particular thermochemical properties of interest.

Functional for Optimization	Species	A_x	A_y	A_z	a_{iso}	T_x	T_y	T_z	ΔT
TPSSH	Co–H	−62.34	−70.89	−15.81	−49.68	−12.66	−21.21	33.87	55.08
TPSSH	*endo*-C–H	29.43	41.37	26.69	32.50	−3.06	8.87	−5.81	14.68

TPSSH	*exo*-C–H	110.51	116.99	111.63	113.05	−2.53	3.94	−1.41	6.47
BP86	Co–H	−62.57	−70.39	−15.81	−49.59	−12.98	−20.80	33.78	54.57
BP86	*endo*-C–H	27.78	39.32	25.16	30.75	−2.97	8.56	−5.59	14.16
BP86	*exo*-C–H	121.99	116.92	115.78	118.23	3.75	−1.31	−2.45	6.21
B3LYP	Co–H	−64.22	−71.97	−15.35	−50.51	−13.71	−21.45	35.16	56.52
B3LYP	*endo*-C–H	25.44	28.28	40.42	31.38	−5.94	−3.10	9.04	14.99
B3LYP	*exo*-C–H	100.81	95.52	94.55	96.96	3.85	−1.44	−2.42	6.27
TPSS	Co–H	−62.62	−70.50	−16.31	−49.81	−12.81	−20.69	33.50	54.18
TPSS	*endo*-C–H	28.63	40.33	25.97	31.64	−3.01	8.68	−5.67	14.36
TPSS	*exo*-C–H	120.13	114.89	113.75	116.26	3.88	−2.51	−1.37	6.39

Table S8: EPR parameters calculated for structures optimized with four different functionals but the same basis sets (def2-SVP(C and H)/def2-TZVP(Co)). Each structure was then used as the input for the calculation of EPR parameters using the same exact conditions (TPSSH/def2-TZVP (C and H)/CP(PPP) (Co)). More detail provided in the general methods section.

Functional for EPR Calculation	Species	A_x	A_y	A_z	a_{iso}	T_x	T_y	T_z	ΔT
TPSSH	Co–H	−62.62	−70.50	−16.31	−49.81	−12.81	−20.69	33.50	54.18
TPSSH	*endo*-C–H	28.63	40.33	25.97	31.64	−3.01	8.68	−5.67	14.36
TPSSH	*exo*-C–H	120.13	114.89	113.75	116.26	3.88	−2.51	−1.37	6.39
BP86	Co–H	−49.16	−57.51	−8.83	−38.50	−10.66	−19.01	29.67	48.68
BP86	*endo*-C–H	30.31	40.07	26.88	32.42	−2.11	7.65	−5.54	13.19
BP86	*exo*-C–H	118.91	112.83	111.61	114.45	4.46	−1.62	−2.84	7.30
B3LYP	Co–H	−91.85	−99.88	−40.50	−77.41	−14.44	−22.47	36.91	59.38
B3LYP	*endo*-C–H	26.86	38.86	24.11	29.94	−3.09	8.92	−5.39	14.75
B3LYP	*exo*-C–H	99.91	107.30	101.6	102.76	−2.84	4.54	−1.70	7.39
TPSS	Co–H	−45.00	−53.02	−4.21	−34.08	−10.92	−18.94	29.87	48.81
TPSS	*endo*-C–H	30.76	41.24	27.76	33.26	−2.50	7.98	−5.49	13.48
TPSS	*exo*-C–H	128.24	123.01	121.84	124.36	3.88	−1.36	−2.52	6.40

Table S9: Structures were optimized using (TPSS/def2-SVP(C and H)/def2-TZVP(Co)). Each structure was then used as the input for the calculation of EPR parameters using different functionals but otherwise the same conditions (def2-TZVP (C and H)/CP(PPP) (Co)).

Discussion of EPR predictions:
We can see when we optimize the isomers with different functionals and then do a single point EPR prediction under the same conditions that the results are nearly identical. When we use different functionals for the single point calculation we see larger differences. However the ΔT and the large disparity in the a_{iso} ($a_{iso} = (A_x + A_y + A_z)/3$) for the *endo*- and *exo*-isomer persist regardless. The performance of TPSSH in predicting the magnitude of a_{iso} was the best so it was selected for use at the higher level of theory (Table S8).

In Table S8, it can be seen that a_{iso} and ΔT are again similar. However, at this level of theory we now also capture that $|T_y|$ is larger than $|T_x|$ or $|T_z|$ in accordance with experiment. The absolute signs of the individual T components are not relevant because we have not determined the absolute sign of the ^1H

hyperfine tensors experimentally. Switching the sign of the hyperfine tensor would switch all of the signs of the components of T as well.

Functional for EPR Calculation	Species	A_x	A_y	A_z	a_{iso}	T_x	T_y	T_z	ΔT
TPSSH	Co–H	−64.18	−72.03	−17.74	−51.32	−12.86	−17.71	33.58	51.29
TPSSH	*endo*-C–H	28.29	40.12	25.82	31.41	−3.12	8.71	−5.59	14.30
TPSSH	*exo*-C–H	116.34	122.51	117.42	118.76	−2.42	3.75	−1.34	5.09

Table S10: Structures were optimized using (TPSS/def2-SVP(C and H)/def2-TZVP(Co). Then a single point calculation was done with CP(PPP) on Co and EPR-III on C and H with grid 7.

S.12 References:

(1) Robbins, J. L.; Edelstein, N.; Spencer, B.; Smart, J. C. Syntheses and electronic structures of decamethylmetallocenes. *J. Am. Chem. Soc.* **1982**, *104*, 1882-1893.

(2) Koelle, U.; Khouzami, F. Permethylated electron-excess metallocenes. *Angew. Chem. Int. Ed.* **1980**, *19*, 640-641.

(3) Del Castillo, T. J.; Thompson, N. B.; Peters, J. C. A synthetic single-site Fe nitrogenase: high turnover, freeze-quench ^{57}Fe Mössbauer data, and a hydride resting state. *J. Am. Chem. Soc.* **2016**, *138*, 5341-5350.

(4) Manson, J. L.; Buschmann, W. E.; Miller, J. S. Tetracyanomanganate(II) and its salts of divalent first-row transition metal ions. *Inorg. Chem.* **2001**, *40*, 1926-1935.

(5) Cazelles, J.; Robert, A.; Meunier, B. Alkylating capacity and reaction products of antimalarial trioxanes after activation by a heme model. *J. Org. Chem.* **2002**, *67*, 609-619.

(6) Hyde, J. S.; Pasenkiewicz-Gierula, M.; Jesmanowicz, A.; Antholine, W. E. Pseudo field modulation in EPR spectroscopy. *Appl. Magn. Reson.* **1990**, *1*, 483-496.

(7) Stoll, S.; Britt, R. D. General and efficient simulation of pulse EPR spectra. *Phys. Chem. Chem. Phys.* **2009**, *11*, 6614-6625.

(8) Sheldrick, G. Crystal structure refinement with SHELXL. *Acta Crystallogr., Sect. C: Struct. Chem.* **2015**, *71*, 3-8.

(9) Dolomanov, O. V.; Bourhis, L. J.; Gildea, R. J.; Howard, J. A. K.; Puschmann, H. OLEX2: a complete structure solution, refinement and analysis program. *J. Appl. Crystallogr.* **2009**, *42*, 339-341.

(10) Neese, F. The ORCA program system. *Wiley Interdiscip. Rev.: Comput. Mol. Sci.* **2012**, *2*, 73-78.

(11) Neese, F. Software update: the ORCA program system, version 4.0. *Wiley Interdiscip. Rev.: Comput. Mol. Sci.* **2018**, *8*, 1327-1332.

(12) Tao, J.; Perdew, J. P.; Staroverov, V. N.; Scuseria, G. E. Climbing the density functional ladder: nonempirical meta-generalized gradient approximation designed for molecules and solids. *Phys. Rev. Lett.* **2003**, *91*, 146401-146404.

(13) Weigend, F.; Ahlrichs, R. Balanced basis sets of split valence, triple zeta valence and quadruple zeta valence quality for H to Rn: design and assessment of accuracy. *Phys. Chem. Chem. Phys.* **2005**, *7*, 3297-3305.

(14) Grimme, S.; Antony, J.; Ehrlich, S.; Krieg, H. A consistent and accurate ab initio parametrization of density functional dispersion correction (DFT-D) for the 94 elements H-Pu. *J. Chem. Phys.* **2010**, *132*, 154104-154119.

(15) Becke, A. D. Density-functional exchange-energy approximation with correct asymptotic behavior. *Phys. Rev. A* **1988**, *38*, 3098-3100.

(16) Perdew, J. P. Density-functional approximation for the correlation energy of the inhomogeneous electron gas. *Phys. Rev. B* **1986**, *33*, 8822-8824.

(17) Becke, A. D. Density-functional thermochemistry. III. The role of exact exchange. *J. Chem. Phys.* **1993**, *98*, 5648-5652.

(18) Lee, C.; Yang, W.; Parr, R. G. Development of the Colle-Salvetti correlation-energy formula into a functional of the electron density. *Phys. Rev. B* **1988**, *37*, 785-789.

(19) Staroverov, V. N.; Scuseria, G. E.; Tao, J.; Perdew, J. P. Comparative assessment of a new nonempirical density functional: molecules and hydrogen-bonded complexes. *J. Chem. Phys.* **2003**, *119*, 12129-12137.

(20) Zhao, Y.; Truhlar, D. G. A new local density functional for main-group thermochemistry, transition metal bonding, thermochemical kinetics, and noncovalent interactions. *J. Chem. Phys.* **2006**, *125*, 194101.

(21) Chalkley, M. J.; Del Castillo, T. J.; Matson, B. D.; Roddy, J. P.; Peters, J. C. Catalytic N_2-to-NH_3 conversion by Fe at lower driving force: a proposed role for metallocene-mediated PCET. *ACS Cent. Sci.* **2017**, *3*, 217-223.

(22) Neese, F. Prediction and interpretation of the ^{57}Fe isomer shift in Mössbauer spectra by density functional theory. *Inorg. Chim. Acta* **2002**, *337*, 181-192.

(23) Barone, V. Structure, magnetic properties, and reactivites of open shell species from density functional and self-consistent hybrid methods In *Recent Advances in Density Functional Methods*; Chong, D. P., Ed.; World Scientific Publishing Co. Pte. Ltd.: Singapore, 1995; Vol. 1, p 287-334.

(24) Klamt, A.; Schüürmann, G. COSMO: a new approach to dielectric screening in solvents with explicit expressions for the screening energy and its gradient. *J. Chem. Soc., Perkins Trans. 2* **1993**, 799-805.

(25) Barone, V.; Cossi, M. Quantum calculation of molecular energies and energy gradients in solution by a conductor solvent model. *J. Phys. Chem. A* **1998**, *102*, 1995-2001.

(26) Cossi, M.; Rega, N.; Scalmani, G.; Barone, V. Energies, structures, and electronic properties of molecules in solution with the C-PCM solvation model. *J. Comput. Chem.* **2003**, *24*, 669-681.

(27) Ribeiro, R. F.; Marenich, A. V.; Cramer, C. J.; Truhlar, D. G. Use of solution-phase vibrational frequencies in continuum models for the free energy of solvation. *J. Phys. Chem. B* **2011**, *115*, 14556-14562.

(28) Wang, T.; Brudvig, G.; Batista, V. S. Characterization of proton coupled electron transfer in a biomimetic oxomanganese complex: evaluation of the DFT B3LYP level of theory. *J. Chem. Theory Comput.* **2010**, *6*, 755-760.

(29) Wu, A.; Mader, E. A.; Datta, A.; Hrovat, D. A.; Borden, W. T.; Mayer, J. M. Nitroxyl radical plus hydroxylamine pseudo self-exchange reactions: tunneling in hydrogen atom transfer. *J. Am. Chem. Soc.* **2009**, *131*, 11985-11997.

(30) Ohki, Y.; Murata, A.; Imada, M.; Tatsumi, K. C−H bond activation of decamethylcobaltocene mediated by a nitrogenase Fe_8S_7 P-cluster model. *Inorg. Chem.* **2009**, *48*, 4271-4273.

(31) Bauer, J.; Braunschweig, H.; Hörl, C.; Radacki, K.; Wahler, J. Synthesis of zwitterionic cobaltocenium borate and borata-alkene derivatives from a borole-radical anion. *Chem. - Eur. J.* **2013**, *19*, 13396-13401.

(32) Yoshida, Z.-i.; Osawa, E. Hydrogen bonding of phenol to π electrons of aromatics, polyolefins, heteroaromatics, fulvenes, and azulenes. *J. Am. Chem. Soc.* **1966**, *88*, 4019-4026.

(33) Cerichelli, G.; Illuminati, G.; Ortaggi, G.; Maria Giuliani, A. The behaviour of ferrocene and ruthenocene in weakly to strongly protic media. Implications on the mechanism of substitutions involving proton as the electrophile. *J. Organomet. Chem.* **1977**, *127*, 357-370.

(34) Chalkley, M. J.; Del Castillo, T. J.; Matson, B. D.; Peters, J. C. Fe-mediated nitrogen fixation with a metallocene mediator: exploring pKa effects and demonstrating electrocatalysis. *J. Am. Chem. Soc.* **2018**, *140*, 6122-6129.

(35) Werner, H.; Lippert, F.; Peters, K.; Schnering, H. G. V. Synthese und Reaktionen der Metall-Base [$(C_5Me_4H)Co(PMe_3)_2$]. *Chem. Ber.* **1992**, *125*, 347-352.

(36) Fang, M.; Wiedner, E. S.; Dougherty, W. G.; Kassel, W. S.; Liu, T.; DuBois, D. L.; Bullock, R. M. Cobalt complexes containing pendant amines in the second coordination sphere as electrocatalysts for H_2 production. *Organometallics* **2014**, *33*, 5820-5833.

(37) Koelle, U. Electrochemistry of transition metal π-complexes. IV. Oxidation of cyclopentadienyl diolefine and cyclobutadiene cobalt complexes. *Inorg. Chim. Acta* **1981**, *47*, 13-18.

(38) Murr, N. E.; Laviron, E. Electrochimie de composés organométalliques. I. Electrosynthèse de cyclopentadiène cyclopentadiényl cobalt substitués. *Can. J. Chem.* **1976**, *54*, 3350-3356.

(39) Green, M. L. H.; Pratt, L.; Wilkinson, G. 760. A new type of transition metal–cyclopentadiene compound. *J. Chem. Soc.* **1959**, 3753-3767.

(40) Belkova, N. V.; Epstein, L. M.; Filippov, O. A.; Shubina, E. S. IR spectroscopy of hydrides and its application to hydrogen bonding and proton transfer studies In *Spectroscopic Properties of Inorganic and Organometallic Compounds: Techniques, Materials and Applications, Volume 43*; Yarwood, J., Douthwaite, R., Duckett, S., Eds.; The Royal Society of Chemistry: Cambridge, UK, 2012; Vol. 43, p 1-28.

(41) Albert, B.; Jansen, M. Zur solvensfreien Darstellung von Tetramethylammoniumsalzen: Synthese und Charakterisierung von $[N(CH_3)_4]_2[C_2O_4]$, $[N(CH_3)_4][CO_3(CH_3)]$, $[N(CH_3)_4][NO_2]$, $[N(CH_3)_4][CO_2H]$ und $[N(CH_3)_4][O_2C(CH_2)_2CO_2(CH_3)]$. *Z. Anorg. Allg. Chem.* **1995**, *621*, 1735-1740.

(42) Berning, D. E.; Noll, B. C.; DuBois, D. L. Relative hydride, proton, and hydrogen atom transfer abilities of $[HM(diphosphine)_2]PF_6$ complexes (M = Pt, Ni). *J. Am. Chem. Soc.* **1999**, *121*, 11432-11447.

(43) Curtis, C. J.; Miedaner, A.; Ellis, W. W.; DuBois, D. L. Measurement of the hydride donor abilities of $[HM(diphosphine)_2]^+$ complexes (M = Ni, Pt) by heterolytic activation of hydrogen. *J. Am. Chem. Soc.* **2002**, *124*, 1918-1925.

(44) Matson, B. D.; Peters, J. C. Fe-rediated HER vs N2RR: exploring factors that contribute to selectivity in $P_3^EFe(N_2)$ (E = B, Si, C) catalyst model systems. *J. Am. Chem. Soc.* **2018**, *8*, 1448-1455.

(45) Warren, J. J.; Tronic, T. A.; Mayer, J. M. Thermochemistry of proton-coupled electron transfer reagents and its implications. *Chem. Rev.* **2010**, *110*, 6961-7001.